MULTIPHASE FLOW MODELING AND ANALYSIS OF PHASED FILLING PROCESS FOR PULSED DETONATION ENGINE

by

NIRMAL KUMAR UMAPATHY

Presented to the Faculty of the Graduate School of

The University of Texas at Arlington in Partial Fulfillment

of the Requirements

for the Degree of

MASTER OF SCIENCE IN AEROSPACE ENGINEERING

THE UNIVERSITY OF TEXAS AT ARLINGTON

DEC 2017

TABLE OF CONTENTS

LIST OF ILLUSTRATIONS

LIST OF TABLES

ABSTRACT

MULTIPHASE FLOW MODELING AND ANALYSIS OF PHASED FILLING PROCESS FOR PULSED DETONATION ENGINES

Nirmal Kumar Umapathy, MS

The University of Texas at Arlington, 2017

Supervising Professor: Frank K Lu

Filling of reactants into a pulsed detonation engine (PDE) should be carried out quickly because any lengthening of the fill time will lead to an increased cycle time. The fill process and, the purge process constitutes a large proportion of time in a cycle. The purpose of this research was to improve the time of fill by implementing various injection geometries in two injection schemes with five different premixed stoichiometric fuel-air mixture injected at wide range of velocity. The different configurations examined were end wall injection, side wall injection with ports angled and normal to the flow direction and staggered side wall injection. The two injection schemes were simultaneous injection and phased injection through side wall ports. The fuel choices were biogas, hydrogen, methane, propane and octane, all in the gaseous state. The oxidizer considered was air and pre-mixed with fuels. Numerical modeling was carried out using the commercial software Fluent™ as the mesh generation tool and flow solver, solving the Reynolds–averaged Navier–Stokes equations with a k–ε turbulence model. The normal sidewall injection yielded the shortest fill time while staggered injection resulted in good fill uniformity. Angled upstream injection resulted in the most advantage with low time of fill, good fill uniformity and moderate spillage. Future improvements were suggested.

NOMENCLATURE

A	Area of cross-section (m^2)
d	Diameter of tube or port (m)
E	Rate of deformation (s^{-1})
f	Frequency of pulse detonation engine (Hz)
k	Turbulent kinetic energy per unit mass (J/kg)
L	Length of chamber (m)
n	Number of inlet ports
$\dot{m}$	Mass flow rate (kg/m^3)
P	Pressure (Pa)
S	Total entropy (J/K)
t	Time (s)
u	Velocity component in axial direction (m/s)
U	Velocity (m/s)
$\forall$	Volume (m^3)
V	Velocity of fill (m/s)
$\bar{V}$	Velocity of phase (m/s)
(x, y, z)	Length components (m)
γ	Phase volume fraction (dimensionless)
Φ	Mixture variable (dimensionless)
ρ	Density of mixture (kg/m^3)
$\bar{\bar{\tau}}$	Diffusion term (N/m^2)

ε	Turbulent dissipation rate (m^2/s^3)
μ	Eddy viscosity ($Pa \cdot s$)
ϕ	Volume fraction (dimensionless)
φ	Spillage (dimensionless)

Subscripts

amb	Ambient
b	Blowdown process
ch	Detonation chamber
CJ	Chapman–Jouguet point
$cycle$	Detonation engine cycle
det	Detonation property
$fill$	Filling of tube
$fuel–air$	Fuel–air mixture
i, j, k	Spatial or temporal index
inj	Injection property
$inlet$	Inlet port
$purge$	Purging process
P	Primary phase
S	Secondary phase
$tube$	Detonation tube

CHAPTER 1

INTRODUCTION

1.1 Background

Of the two modes of combustion, namely deflagration and detonation, it is the latter which is the more efficient means of converting the chemical energy content of the fuel [1]. However, the use of detonation in constructive ways has been explored in earnest only from the second half of the twentieth century [2]. The primary application was aimed toward aerospace propulsion. In chronological order, the various engine concepts developed based on detonation are oblique detonation wave engines (ODWEs) [3, 4] followed by pulsed detonation engines (PDEs) [5, 6, 7] and later rotating detonation engines (RDEs) [8].

The PDE remains of interest. The reasons include simplicity in design, ease of manufacture and compactness. Typically, in a PDE, the combustion mixture is filled in a tube with one end open and the other closed from which the detonation wave is initiated. Thrust is generated by the rapid rise in pressure and the momentum flux created by the hot gases. This process cycles at a high frequency which generates quasi-steady thrust [9].

1.2 Detonation

Detonation, from the Latin *detonare*, meaning 'to thunder down,' is an extremely rapid way of material and energy conversion. Detonation differs from deflagration by the way the energy is converted. In a deflagration, the energy is converted through heat from a hot burning material to the next layer of cold material which is

then ignited to release chemical energy; in other words, through heat conduction. On the other hand, the energy transfer in detonation takes place through a strong shock wave that rapidly heats the material by compression. This compression, which raises both pressure and temperature, triggers chemical reactions to take place rapidly, forming a strong compression wave coupled to a combustion front which together is known as the detonation wave. The detonation wave is sustained spontaneously by the energy from the reaction zone behind the shock that sends compression waves upfront and keeps the detonation wave from decaying. The detonation process is three to eight orders of magnitude faster in nature than deflagration [10].

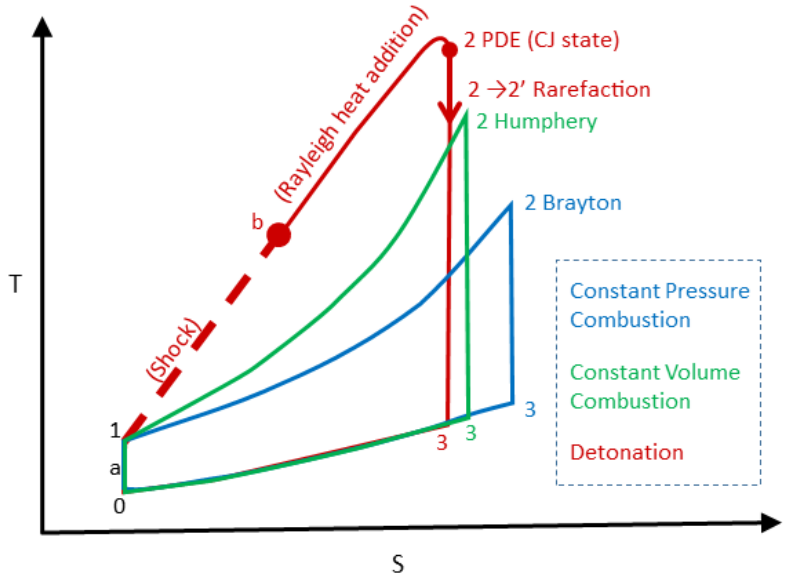

Figure 1.1. T–s diagram of ideal cycles: Humphrey, Brayton and detonation cycle (based on [2]).

Figure 1.1 illustrates the thermodynamics of the detonation cycle in comparison to the Humphrey (constant-volume combustion) and Brayton (constant-pressure combustion) cycles. The process $0 \rightarrow 1$ is a reversible compression which is an inherent

part of the Brayton cycle, but not required for either the Humphrey or the detonation cycles. From point 1, the temperature of the gas is increased due to compression of the shock wave to an intermediate point. This initiates the chemical combustion or detonation. To be pertinent, only the detonation cycle is briefly discussed below.

For cycle analysis, consider a detonation wave initiated at the closed end of the tube filled with combustible gas mixture. The tube is assumed to be open at the other end towards which the detonation wave propagates. The detonation wave rapidly compresses the fuel and causes detonation. In the detonation cycle, temperature is increased drastically through a supersonic Rayleigh process accompanied by a decrease in pressure. The pressure peak before the drop is known as the von Neumann spike. The gas undergoes complete combustion up to stage 2, which is known as the Chapman–Jouguet (CJ) condition for self-sustaining detonation, also known as the upper CJ point. Henceforth, chemical equilibrium is attained and the flow relative to the detonation wave front is sonic [11]. The detonation wave velocity and the CJ properties can be computed analytically or obtained using tools such as the NASA CEA applet [12].

At point 2, the pressure and temperature as well as the density of gas are substantially higher than at point 1. This is accompanied by the subsequent development of an unsteady expansion wave behind the detonation wave known as Taylor rarefaction. Moreover, unsteady rarefaction waves are generated from the closed end of the tube. The expansion leads to a decrease in pressure in the burnt gas [13]. The cycle is completed through an imaginary constant static-pressure process in which the excess heat is removed to the surroundings from the exhaust [11].

1.3 PDE Gas Dynamics Processes

The pulse detonation engine, as mentioned earlier, operates in cycles producing quasi-steady thrust. The pulsing phenomenon is due to the time between each rapid detonation stage accompanied by comparatively slower fill and purging stages. The schematic in Fig. 1.2 shows a typical PDE with two injection ports. For simplifying the discussion, the velocity at the inlet ports is assumed to be uniform.

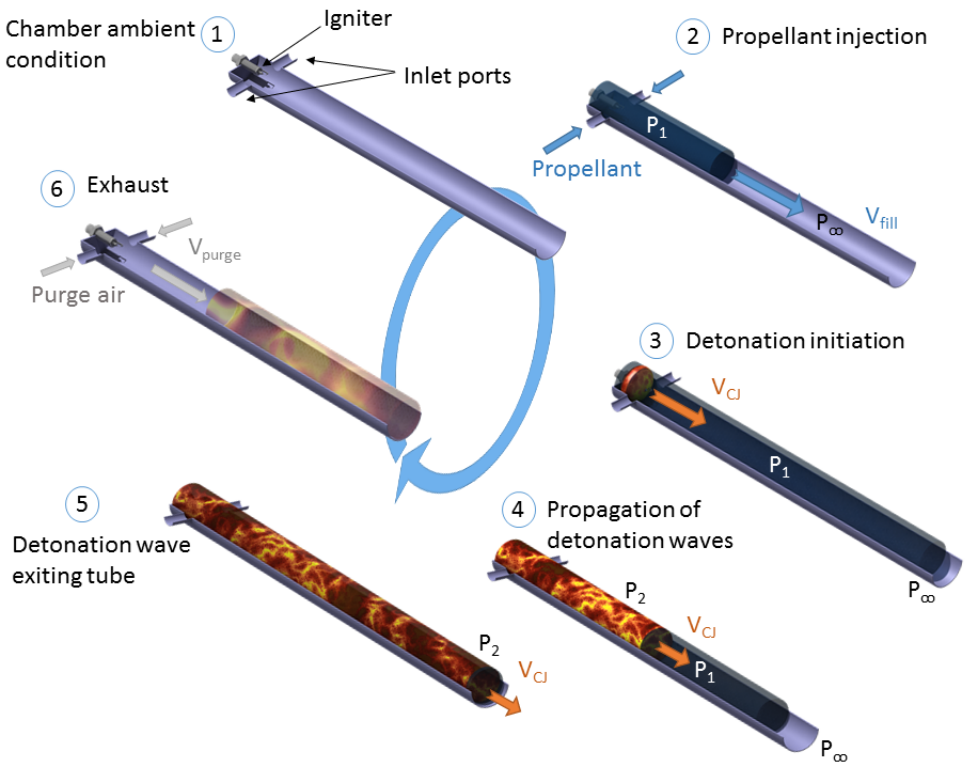

Figure 1.2. Key stages of a PDE cycle (based on [2]).

Figure 1.2 shows the igniter positioned for initiation from the closed end towards the open end. In reality, the region near the closed end hosts devices that speeds up the so-called deflagration-to-detonation transition process. To simplify this discus-

sion, the mechanisms that nurture DDT are not shown and it is assumed that DDT is achieved over a very short length and time.

Going clockwise from 1 to 6, the chamber is initially at ambient condition, i.e., it is filled with air at P_{amb} and T_{amb}. The reactants are injected through inlet ports and they propagate towards the open end and fill the tube in time t_{fill}, following which, the detonation is initiated from the closed end of the tube through the igniter. The detonation wave propagates through the tube feeding on the reactant gases at a velocity V_{det}. It propagates through the tube in a time t_{det}. Once the detonation reaches the end of the tube, it induces an unsteady expansion to propagate into the chamber. This is followed by scavenging of the tube with cool, purge air at a velocity of V_{purge}. Sccavenging of the tube by cool air is critical to prevent autoignition of the fuel. A brief discussion of each process is given below.

1.3.1 Filling Cycle

The empty tube in step 1 is filled through one or a number of inlet ports. Step 2 shows the filling cycle. The time taken to fill the entire volume of detonation chamber with reactants is denoted as t_{fill}. The filling is assumed to be ideal, i.e., the mass of reactants injected through the inlet is equal to the mass of reactants inside the tube. This is known as a filling ratio of unity. It is possible to over- or underfill the chamber. For a filling ratio of unity and assuming ideal filling conditions,

$$t_{fill} = \frac{\forall_{tube}}{V_{fill} \sum_{1}^{n} A_{inlet}} \tag{1.1}$$

where $\forall$ is the volume of the detonation tube, n is the number of inlets all of which have the same cross-section area A_{inlet}.

1.3.2 Detonation Cycle

At the end of the filling process, the reactants are ignited from the closed end of the tube. Various methods have been proposed for igniting the mixture but the common approach is to use an automotive spark plug; stage 3 in Fig. 1.2. The energy produced by a spark plug is insufficient to cause a direct detonation initiation which requires an exorbitant amount of energy. The spark plug in fact initiates a deflagration which is then accelerated to a detonation in a short distance through a deflagration-to-detonation (DDT) transition device such as a Shchelkin spiral [14]. The wave propagation is illustrated as stage 4 in Fig. 1.2. The propagation time of the detonation wave, even though a portion of it is actually a deflagration, is extremely short compared to the fill time or the blowdown time (to be discussed later). Thus, this time can be safely neglected for estimating the overall cycle time. Stage 5 in Fig. 1.2 shows the wave exiting the tube. In passing it can be noted that the cycle time can be shortened by triggering the detonation before the reactants reach the open end [15]. This is done by careful timing of valves and ignition in such a way that the injected reactants and the detonation wave reach the open end at the same time.

The time for the ideal detonation wave to exit the detonation tube can be expressed as

$$t_{det} = \frac{L_{tube}}{V_{CJ}} \tag{1.2}$$

This time is independent of the volume of the chamber if the length-to-diameter ratio is high. This implies that the wave front is one dimensional.

1.3.3 Blowdown Cycle

The detonation wave travels faster than the burning gases and leaves behind hot combustion products inside the chamber. The gases inside the chamber exhibit

a range of velocities. For example, the gas is at rest at the closed end whereas it is locally sonic behind the detonation wave. Moreover, there is also a whole range of variation of gas temperature, pressure and density. The pressure difference is associated with an unsteady rarefaction that travels from the exit toward the closed end at the local sonic velocity of the burnt gas, followed by an unsteady compression system. This blowdown process of unsteady rarefaction and compression brings the chamber to ambient pressure with residual heat on the walls. The time for blowdown stage is empirically estimated to be [15]

$$t_b = \frac{4L_{tube}}{V_{CJ}} \tag{1.3}$$

1.3.4 Purge Cycle

The blowdown process restores the pressure and velocity in the chamber back to ambient and zero respectively. However, the residual heat on the chamber walls and in the combustion products left within chamber poses a practical difficulty on the successive cycle. This is because the temperature may be above the autoignition temperature that will result in instant deflagration. Therefore, before the next charge of reactants is introduced, cold air is injected into the detonation tube to scavenge the burnt products as well as help in the cooling the chamber walls. If the purge air is introduced through a similar number of ports and comparable velocity as the reactants, then the purge time will be approximately equal to the fill time t_{fill}, namely,

$$t_{purge} = \frac{\forall_{tube}}{V_{fill} \sum_{1}^{n} A_{inlet}} \tag{1.4}$$

1.3.5 Cycle Time

The PDE cycle time is the summation of the time taken for the above four processes although in practice the total time may be longer or shorter. This is because some designs incorporate cycles that overlap in time and some require time delays between each of these cycles. In cases where the fill time is rapid, the initiation is done before reactants reach the open end of the tube. Also, the purging process at one part of tube may take place simultaneously while the filling is done elsewhere in the chamber. These features may be found in a rapid fill configuration such as when the reactants are injected from the side walls. The generic cycle time can then be written as a direct summation:

$$t_{cycle} = t_{fill} + t_b + t_{det} + t_{purge} \tag{1.5}$$

1.4 Typical PDE Cycle Time

Early studies have shown that the PDE for aerospace applications should operate at frequencies of 50–100 Hz, which leads to a cycle time of 10–20 ms [15]. In the extensive discussion of the cycles above, the time taken for detonation t_{det} is very short due to the high detonation wave velocity. The time for blowdown is effectively considered to be four times that of the time for detonation t_{det} which also makes its contribution to be marginal to the overall cycle time.

To better understand the above, a simplified PDE layout with end filling is considered. Assume that the closed end of tube is the inlet port, i.e., the diameter of detonation tube is equal to the diameter of inlet tube. Consider a tube of 100 mm

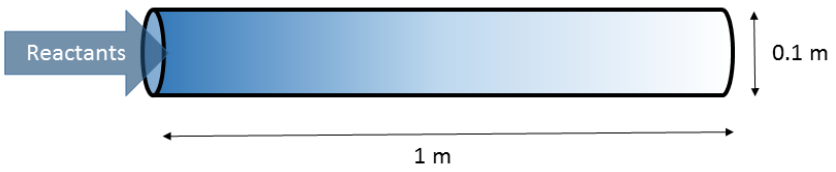

Figure 1.3. Schematic of PDE considered.

diameter and 1 m length, with inlet filling velocity of 50 m/s and ambient conditions at the outlet. Thus, from Eqn. (1.1) with $n = 1$

$$t_{fill} = \frac{\forall_{tube}}{V_{fill} A_{inlet}} = \frac{\cancel{A_{inlet}} L_{tube}}{V_{fill} \cancel{A_{inlet}}} = \frac{L_{tube}}{V_{fill}} = \frac{1}{50} = 2 \times 10^{-2} = 0.02 \text{ s} \tag{1.6}$$

The time of filling alone is 0.02 s and with an equivalent purge time yields a cycle time of 0.04 s or equivalently a frequency of 25 Hz which falls short of the frequency requirement of 50–100 Hz. It is evident that this time must be reduced to achieve the desirable operation frequency range. Reducing the cycle time can be achieved through either increasing the injection velocity at the inlet or increasing the number of ports.

To complete the analysis, the time for detonation wave propagation with a CJ velocity for a stoichiometric H_2–O_2 mixture at STP of 2836 m/s is given from Eqn. (1.2) to be

$$t_{det} = \frac{1}{2836} = 3.5 \times 10^{-4} \text{ s} \tag{1.7}$$

This is two orders less than the time taken for filling and is pertinent to the previous discussion on the contribution of t_{det} on the cycle time.

Moving further, from Eqn. (1.4), the time for blowdown is

$$t_b = 4t_{det} = 1.4 \times 10^{-3} \text{ s} \tag{1.8}$$

After the blowdown, the detonation tube is cooled and exhaust is scavenged out through a purging cycle. In this case, the purging is done through the inlet port. Therefore, the time taken for purging is equal to the fill time, namely,

$$t_{purge} = t_{fill} = 2 \times 10^{-2} \text{ s} \tag{1.9}$$

Finally, from the above, the overall cycle time can be obtained by summation of individual process times:

$$\begin{aligned} t_{cycle} &= 2 \times 10^{-2} + 3.5 \times 10^{-4} + 1.4 \times 10^{-3} + 2 \times 10^{-2} \\ &= 4.176 \times 10^{-2} = 41.76 \text{ ms} \end{aligned} \tag{1.10}$$

The t_{cycle} above is equivalent to a frequency of 23.9 Hz which is lower than the required range of 50–100 Hz for application in aerospace propulsion.

The proportion of the contributions of the four processes can be visualized from the infographic presented in Fig. 1.4. This figure shows vividly that majority of time is taken by the purging and filling processes. Also, the time of detonation and blowdown is a trait of length and geometry of detonation tube. This shows the importance of reducing the filling and purging times to facilitate high-frequency operation. The present work concentrates on reducing the time of filling by increasing the flow rate of inlet and the number of ports.

Filling the tube at a higher flow rate may be desirable but this incurs large pumping requirements, adding to the complexity, volume and weight. Increasing the velocity increases the power requirements by the cube of velocity. Thus, the simple

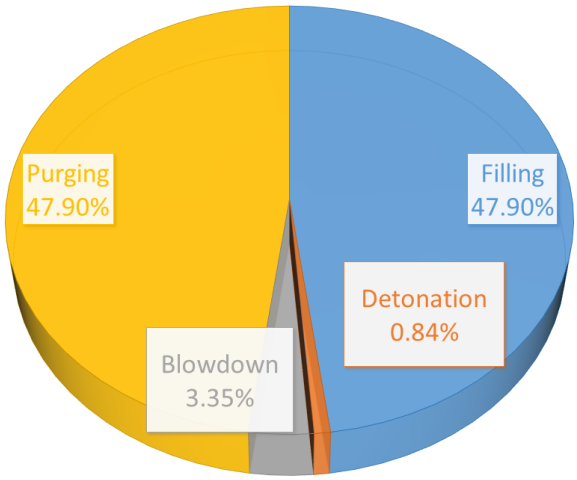

Figure 1.4. Time of each cycle, in percentage, for a typical PDE and their relative contributions on the total cycle time.

correlation above shows conflicting requirements between achieving high frequency and the limitation of increasing the velocity of inlet flow.

Further, scavenging may create "dead air" regions within the detonation chamber. These are pockets of burnt gases that are trapped within the fresh stream of fuel-air mixture or purged air. The dead air region can lead to auto ignition of fuel–air mixture within the detonation chamber due to the relatively higher temperature of these gas pockets. Also, the detonation wave is sustained by the constant combustion of the fuel-air mixture and any discrepancy in the mixture can result in erratic wave propagation. This can diminish PDE performance or may even cause misfires.

In view of the conflicting requirements mentioned above, a numerical study was performed on alternative fill strategies. Rather than increasing the flow rate exorbitantly, the idea is to place several inlets on the sidewall to improve the overall mass flow into the engine. This approach aims to address the issue of increasing the mass flow without increasing pressure and also possibly for reducing dead-air regions.

To reduce dead air regions, the purging cycle should be carried on until the trapped dead air region is scavenged out. In this process, some portion of the reactants may escape from the open end, which is termed as spillage, and the volume associated with it as volume of spillage. This is detrimental to the performance of the PDE since it increases the amount of reactants required, and therefore time of fill, to compensate for the additional reactants that are spilled out. Apart from the impact it has on the efficiency, the spillage of reactants is hazardous. Therefore, spillage is one of the key traits that must be taken into consideration while designing the rapid fill inlet configuration. The above issues, apparently, have not been well addressed in literature.

These phenomena are difficult to study experimentally but are amenable to numerical analysis. The overall concept is that, if extra ports are available for sidewall filling, the tube can be filled more rapidly and efficiently. Different sidewall filling configurations were studied. A part of the study also varied the fill rate, position of inlet port, angle of injection and timed dependent injection. Finally, different stoichiometric, pre-mixed gaseous fuels and air were used to fill the tube. To help characterize the fill performance, the following performance metrics were considered, namely, (i) the time for the volume to be filled up to 90 percent, (ii) spillage ratio and (iii) quality of fill.

CHAPTER 2

Methodology

2.1 Multiphase Flows

To compute the filling process of a PDE, the numerical modeling must be carried out employing more than one material phase. For the filling process, the injected fuel–air, reactant mixture and the air initially in the tube are non-reactive. The presence of more than one material in the same or different physical states of matter allow for the solving of the purging process through multiphase flow solvers [16]. The different materials in a multiphase flow field can be represented as primary and secondary phases. The interface between the two phases in the present study is gas–gas and the model is briefly discussed later. The primary (also known as continuous) phase is air. The secondary (or distributed) phase is the gaseous reactant mixture.

2.2 Approaches in Multiphase Modeling

The multiphase flow can be solved using two approaches, the Euler–Lagrange or the Euler–Euler approach. Both techniques have distinctive solution methods and are capable of solving diverse multiphase flow fields [17]. It is necessary to identify the one that is well suited for the current study.

2.2.1 Euler–Lagrange Approach

In this approach the primary fluid phase is solved using the Navier–Stokes equations, treating it as a continuum. The secondary phase is calculated by tracking particles within the primary phase. The momentum, mass and energy of both

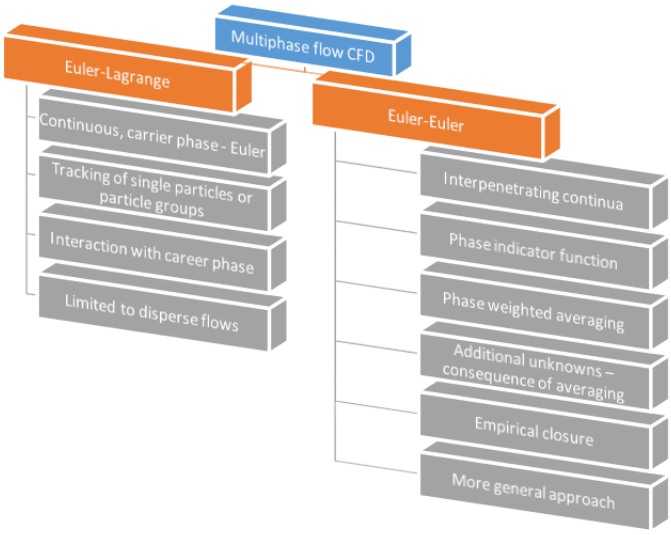

Figure 2.1. Multiphase modelling based on [17].

the phases are exchanged. This method is accurate only when the volume fraction of secondary phase is less than 10 percent of the primary phase. In other words, the interaction of the secondary phase with primary phase is totally neglected when the volume fraction of secondary phase exceeds 10 percent. This type of multiphase model is suitable for flows of spray dryers, some particle laden flows and, as mentioned previously, will not be suitable for cases where the secondary phase occupies a comparable volume as the primary phase.

2.2.2 Euler–Euler Approach

This method assumes that the multiphase flow is comprised of interpenetrating continuum. The volume occupied by one phase cannot be occupied by the other,

therefore, this method uses a quantity known as the volume fraction. The summation of the volume fraction within the domain is unity. The physical meaning is that a fraction of space is occupied by each of the phases. A conservation equation is derived for every single phase to obtain a set of equations with the same structure for all phases. The equations are closed by providing constitutive relations that are obtained from empirical information or using kinetic theory for granular flows. The Euler–Euler approach is further classified into three different approaches as depicted in Fig. 2.2.

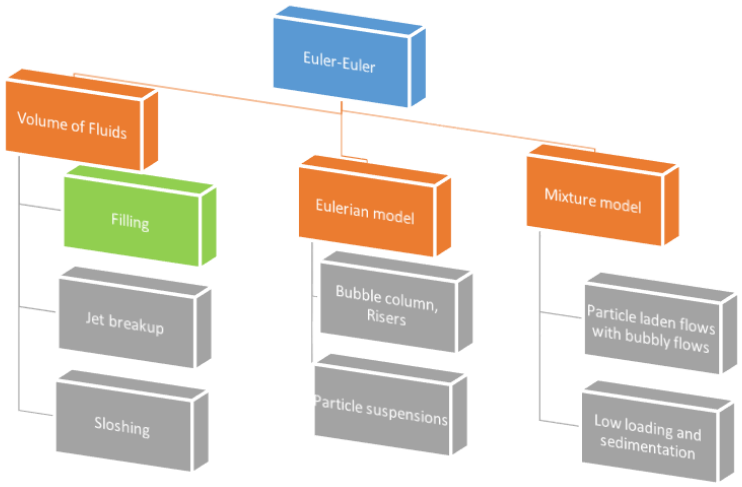

Figure 2.2. Euler–Euler approaches with application.

2.2.2.1 Volume of Fluid Model

The "volume of fluid" (VOF) approach is a surface tracking method applied to a fixed Eulerian mesh. This is the widely-used multiphase approach [18] in cases where the interface between the fluids is of maximum interest [19]. A single momentum equation is shared by fluids based on their relative volume fractions in each computation and is tracked over the entire domain. This approach is useful in the analysis of filling, prediction of jet breakup and sloshing.

2.2.2.2 Eulerian Model

The Eulerian model is the most complex approach compared to other multiphase solver approaches. It solves a number of momentum and continuity equations for each phase, coupled through the pressure and interface exchange coefficient. The latter is obtained through the kinetic theory for granular flows (fluid–solid). The method is widely used for bubble columns, risers and particle suspensions. More discussion on the method is found on [20].

2.2.2.3 Mixture Model

The mixture model is used with discrete phases, as with the Eulerian model. The phases are treated as interpenetrating continuum. The mixture momentum equation is solved and the relative velocities are prescribed to the dispersed phases. This model is commonly used for particle laden flows with bubbly flows, low loading and sedimentation. This is also used to solve homogeneous multiphase flows.

Based on the above discussion, the VOF model is the most suitable method which allows the computation of flow in which the volume fraction of primary and

secondary phases change drastically. Also, it is the most widely-used model for filling analysis.

2.2.3 Time Scheme for Multiphase Flows

To accurately model the physics of the multiphase flow, a very high resolution is required both temporally and spatially. Fluent™ has first-order temporal schemes for all the models and second-order temporal schemes for all models except the VOF explicit scheme introduced in section 2.2.7.

The second-order temporal scheme is used in all the time discretizations in the present work, starting with the transport equations, energy equations, species transport equations, turbulence model, phase volume fraction equations to the pressure correction equations. This provides very accurate modeling of the physics between two infinitesimally small time steps.

The transport equation in multiphase flow is written as follows

$$\frac{\partial}{\partial t}\left(\gamma\rho\phi\right) + \nabla\left(\gamma\rho\bar{V}\Phi\right) = \nabla\bar{\bar{\tau}} + S_{\Phi} \tag{2.1}$$

where ρ is the density of the mixture phase, Φ is the mixture variable or phase variable, γ is the phase volume fraction, $\bar{V}$ is the velocity of the phase and $\bar{\bar{\tau}}$ is the diffusion term. A second-order, time accurate implicit scheme is used for time stepping. The scheme is unconditionally stable but a larger time step results in oscillatory solutions.

2.2.4 VOF Approach

The VOF approach is applied with the assumption that the phases are not interpenetrating. For every phase in the model, a variable known as the volume fraction of that phase is introduced. This value is calculated for each phase over every single cell which is eventually added to find the volume fraction of a phase/material

in the entire domain. In each control volume, the volume fractions of all the phases obviously sum to unity. The field variables in each cell are shared with all the phases and represent the volume averaged values. The properties and variables in any given cell are either a representation of a mixture of phases or purely representative of one of the phases, determined by the volume fraction of the cell. If a fluid possesses γ_p volume fraction in a cell, then the following conditions may exist for different values of γ_p:

$\gamma_p = 0$	Cell is devoid of fluid p
$0 < \gamma_p < 1$	Cell has interface between fluid p and one or more fluids
$\gamma_p = 1$	Cell is full of fluid p

An illustration of the above is provided in Fig. 2.3.

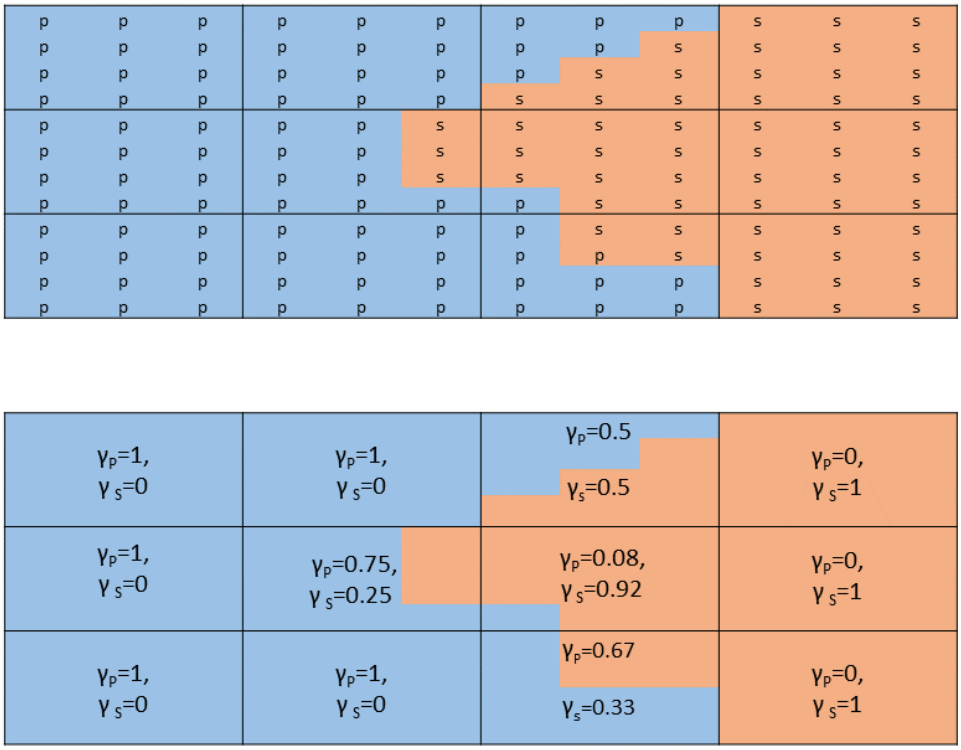

Figure 2.3. Volume fraction schematics representing each cell with 12 face center and corresponding change in γ values.

2.2.5 Solution Method for VOF

The continuity equation for the volume fraction of one or more phases has to be solved to track the interface between the phases. The continuity equation for phase p may be written as

$$\frac{1}{\rho_p}\left[\frac{\partial}{\partial t}\left(\gamma_p \rho_p\right) + \nabla\left(\gamma_p \rho_p \vec{v}_p\right) = S_{\gamma_p} + \sum_{s=1}^{n}(\dot{m}_{sp} - \dot{m}_{ps})\right] \tag{2.2}$$

where $\dot{m}_{sp}$ is the mass transfer from the s to the p phase and $\dot{m}_{ps}$ is the mass transfer from the p to the s phase. The source term S_{γ_p} is zero for flows with zero mass transfer. The volume fraction of the secondary phase s is solved to yield the volume fraction of the primary phase p by

$$\sum_{p=1}^{n} \gamma_p = 1 \tag{2.3}$$

The above relations can either be solved implicitly or explicitly based on the time discretization that is adopted.

2.2.6 Implicit Scheme

The implicit scheme in Fluent™ uses the software's standard finite difference interpolation scheme and employs the following formulations for interface capturing, namely, QUICK, second-order upwind, first-order upwind and modified HRIC schemes or MHRIC (modified refined high resolution intertace capturing). The MHRIC scheme is well suited for these kinds of simulations where the primary and secondary interface are in the same physical state. Other other schemes for interface capturing are the compressive interface capturing scheme for arbitrary meshes (CICSAM) [21] and HRIC. These provide a good background to understand the MHRIC

scheme. MHRIC is employed for implicit interface capturing in current research. The implicit time discretization of Eqn. (2.2) is given below:

$$\frac{\gamma_p^{n+1}\rho_p^{n+1} - \gamma_p^n \rho_p^n}{\Delta t}\forall_{cell} + \sum_f (\rho_p^{n+1} U_f^{n+1} \gamma_{p,f}^{n+1}) = \left[S_{\gamma_p} + \sum_{s=1}^{n} (\dot{m}_{sp} - \dot{m}_{ps}) \right] \forall_{cell} \quad (2.4)$$

The above equation requires the volume fraction at the current time step. Therefore, a standard scalar transport equation is solved iteratively to compute the volume fraction at the current time.

2.2.7 Explicit Scheme

The explicit scheme available in Fluent™ is a standard, finite difference interpolation scheme. The explicit time discretization of Eqn. (2.2) is given below:

$$\frac{\gamma_p^{n+1}\rho_p^{n+1} - \gamma_p^n \rho_p^n}{\Delta t}\forall_{cell} + \sum_f (\rho_p^{n} U_f^{n} \gamma_{p,f}^{n}) = \left[\sum_{s=1}^{n} (\dot{m}_{sp} - \dot{m}_{ps}) + S_{\gamma_p} \right] \forall_{cell} \quad (2.5)$$

The explicit scheme has the same formulation as the implicit scheme to obtain the face fluxes. But, the explicit scheme requires only the values of volume fraction at the previous time step therefore it does not require any iterative solution within a time step.

2.2.8 VOF Scheme Adopted

Based on the discussions in section 2.2.3, 2.2.6 and 2.2.7, it is necessary to decide on the scheme that would be most suitable for the present case. The temporal scheme has a huge role to play over the entire computation of transient simulations. Considering the fact that Fluent™ supports only first-order time discretization for explicit multiphase schemes, it would be necessary to maintain very small grids and time steps to capture the physics. This requires huge and thus costly computational time. On the other hand, an implicit scheme needs a number of iterations within each

time step but is capable of second-order accurate time discretization. Therefore, it is more accurate and the time step size can be relaxed given the fact the solution will converge within each time step.

Practically, the implicit or the explicit scheme may not differ in computation time given the fact an explicit scheme has more time steps (due to smaller time step size) while an implicit scheme has a large number of iterations for a lesser number of time steps. Often the choice of scheme depends more on the researcher's preference than the solver. Previous work on the related topic [15] was carried out an using explicit formulation. The current work is carried out fully on an implicit solver and the solver settings will be discussed subsequently.

2.3 Turbulence Models

Turbulence models are used to address the turbulence closure problem in solving the Navier–Stokes equations. Reynolds-averaging the Navier–Stokes equations gives rise to RANS (Reynolds-averaged Navier–Stokes) equations. Due to the non-linearity of the Navier–Stokes equations, the fluctuations in velocity manifests as a non-linear term $-\rho\overline{v_i' v_j'}$ known as the Reynolds stresses [22]. In order to get the mean velocity and pressure, it is necessary to close the RANS equations through modeling the Reynolds stress term without any reference to the fluctuating component of the velocity.

Fluent™ has twelve turbulence models. The commonly used models for multi-phase modeling are two-equation models, namely, k–ε and k–ω as well as the seven-equation model known as the Reynolds stress model (RSM). The k–ε and k–ω turbulence models are considered for the current work. These lower-order models are chosen to reduce the computation cost.

2.3.1 k–ε Model

The k–ε model is based on the assumption that the ratio of the Reynolds stress and the mean rate of deformation is the same in all directions. This is a two-equation model, where k denotes the turbulent kinetic energy which is, in other words, the energy contained in the turbulence, and ε which is the turbulent dissipation and used to calculate the rate of dissipation of turbulent kinetic energy [23].

The equation for the turbulent kinetic energy k can be written as

$$\frac{\partial}{\partial t}(\rho k) + \frac{\partial}{\partial x_i}(\rho k u_i) = \frac{\partial}{\partial x_j}\left(\frac{\mu_t}{\sigma_k}\frac{\partial k}{\partial x_j}\right) + 2\mu_t E_{ij}E_{ij} - \rho\varepsilon \tag{2.6}$$

while the equation for dissipation ε can be written as

$$\frac{\partial}{\partial t}(\rho \varepsilon) + \frac{\partial}{\partial x_i}(\rho \varepsilon u_i) = \frac{\partial}{\partial x_j}\left(\frac{\mu_t}{\sigma_\varepsilon}\frac{\partial \varepsilon}{\partial x_j}\right) + C_{1\varepsilon}\frac{\varepsilon}{k}2\mu_t E_{ij}E_{ij} - C_{2\varepsilon}\rho\frac{\varepsilon^2}{k} \tag{2.7}$$

where u_i is the Cartesian velocity component, E_{ij} is the rate of deformation, μ_t is the eddy viscosity and σ_k, σ_ε, $C_{1\varepsilon}$,$C_{2\varepsilon}$ are adjustable constants. Though the model can capture turbulence well, the isotropic assumption for eddy viscosity makes it unsuitable for computation of flows in inlets, curved boundary-layer flow and rotating flows [24].

2.3.2 Realizable k–ε Model

The realizable k–ε has an additional variable C_μ. This method has superior capability to allow for the spreading rate in planar and round jets as well as flows involving rotation, re-circulation and adverse gradients. Similar to the k–ε formulation, the turbulent kinetic energy equation for the realizable k–ε is written as [23]

$$\frac{\partial}{\partial t}(\rho k) + \frac{\partial}{\partial x_i}(\rho k u_i) = \frac{\partial}{\partial x_j}\left[\left(\mu + \frac{\mu_t}{\sigma_k}\right)\frac{\partial(k)}{\partial x_j}\right] + p_k + P_b - \rho\varepsilon - Y_M + S_K \tag{2.8}$$

Also the equation for dissipation ε can be written as

$$\frac{\partial(\rho\varepsilon)}{\partial t}+\frac{\partial(\rho\varepsilon u_i)}{\partial x_i}=\frac{\partial}{\partial x_j}\left[\left(\mu+\frac{\mu_t}{\sigma_\varepsilon}\right)\frac{\partial(\varepsilon)}{\partial x_j}\right]+\rho C_1 S_\varepsilon-\rho C_2\frac{\varepsilon^2}{k+\sqrt{\nu\varepsilon}}+C_{1\varepsilon}\frac{\varepsilon}{k}C_{3\varepsilon}P_b+S_\varepsilon \tag{2.9}$$

where P_k represents the turbulent kinetic energy generation due to the mean velocity and P_b is the generation of turbulent kinetic energy due to buoyancy. The rest of the terms are calculated in the same way as in the k–ε model.

Previous work on rapid filling of PDE [15] was carried out using the realizable k–ε turbulence model. Also, background study on the k–ω turbulence model showed that it suffers the same inherent disadvantage as the k–ε model as it considers μ_t to be isotropic. Therefore, the realizable k–ε was used to model turbulence in the current study.

2.4 Numerical Modeling

2.4.1 Computational Approach

The computation of flow includes various stages before the actual governing equations can be solved. The effective way of modeling the physical conditions into a mathematical model known as the pre-processing phase is carried out first. Once the problem is defined mathematically and discretized, the governing equations are solved iteratively towards a converged solution. After the solution is attained, it is necessary to represent the mathematical values back into the physical space to infer results, known as the post-processing phase. A limited discussion is made on the computational methodology and more information can be found on the related references mentioned in each subsection.

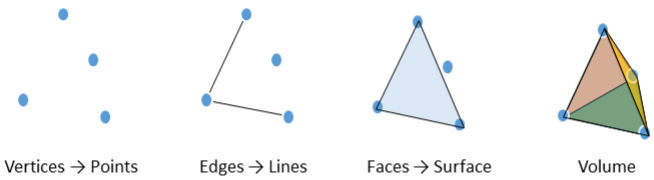

Figure 2.4. Bottom-up geometry methodology for a basic tetrahedron.

2.4.2 Geometry

The geometry can be modeled by two different approaches, the first being the top-down approach where the computational domain is created by logical operations on primitive shapes such as cylinders, cubes and spheres. This is not widely used as it is impossible to model complex geometries. The second approach is known as the bottom-up approach and this refers to a methodology where the vertices are first defined and are then connected by lines to form edges. Three or more edges combine to form a closed contour known as face and four or more faces combine to form a volume. In the current work, the geometry is created using bottom-up approach shown in 2.4. The pre-processor application in Fluent™ known as geometry modeler is extensively used to generate geometries. The physical representation of the rapid fill models are generated using the CAD package CATIA™ V5 R20.

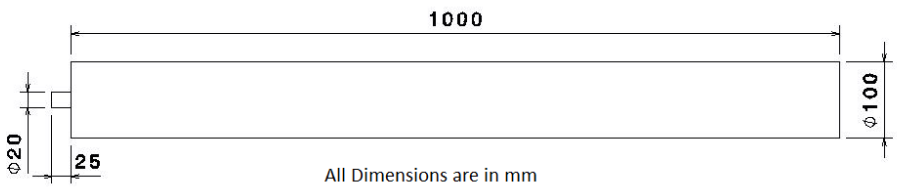

Figure 2.5. Geometry of case–1 fill configuration.

A detonation tube of 1 m length and 0.1 m diameter is considered. The tube is filled through different inlet configurations, the inlet port dimensions are kept at a constant 0.02 m diameter [25]. The upstream details of injector ports are neglected. The geometry of the various configurations are detailed below.

Case 1

Case 1 is the simplistic approach of injecting reactants from the end wall as shown in Fig. 2.5. The inlet port is centered at the end wall. This configuration is studied as a baseline to compare with other rapid fill configurations.

Case 2

Case 2 has a single end-wall port and array of four pairs of opposing sidewall ports as shown in Fig. 2.6. Such a configuration with opposing impinging jets can possibly fill the tube faster. A sidewall injection concept was proposed previously [26] and was applied to a large PDE ground demonstrator [14]. In the present study, all the side fill cases utilize eight side ports with the end port kept to minimize dead air pockets at the closed end. The number and spacing of the ports were chosen based on the feasibility of actual fabrication, installation and operation.

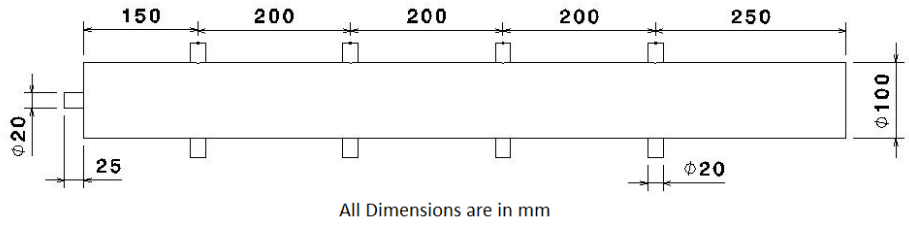

Figure 2.6. Geometry of case 2 rapid fill configuration.

Case 3

Case 3 has a single end-wall port and an array of four pairs of opposing sidewall ports inclined downstream at 45 degrees as shown in Fig. 2.7. Case 3 is considered a possible candidate for filling the tube rapidly.

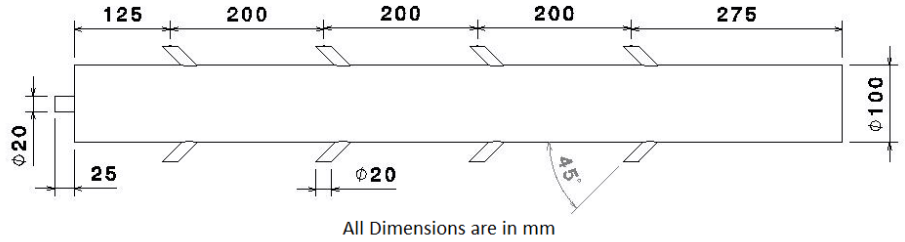

Figure 2.7. Geometry of case 3 rapid fill configuration.

Case 4

Case 4 has a single end-wall port and an array of four pairs of opposing sidewall ports inclined upstream at 45 degrees as shown in Fig. 2.8. This configuration is thought to be able to rapidly fill dead air regions.

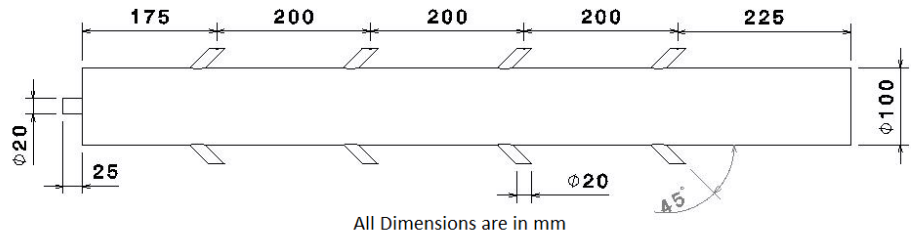

Figure 2.8. Geometry of case 4 rapid fill configuration.

Case 5

Case 5 has a single end-wall port and an array of seven inlet ports arranged in a staggered manner along the streamwise direction in sidewall as shown in Fig. 2.9. This is considered as a possible candidate for rapid filling with good uniformity of fill as the ports are spread well in the streamwise location.

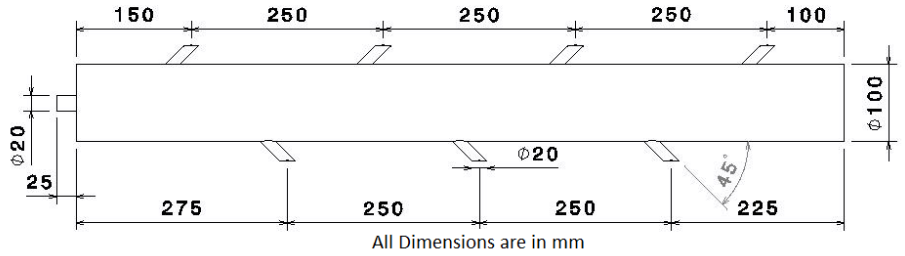

Figure 2.9. Geometry of case 5 rapid fill configuration.

2.4.3 Grid Generation

A grid is a discrete representation of the actual geometry of the problem. The discretized governing equations are solved at these points. The quality of the grid has a big impact on the rate of convergence and sometimes on the convergence itself.

It obviously plays a phenomenal role in the accuracy of solution. Grids are classified into three categories as described briefly below.

Structured Grid

A structured grid has a regular or uniform continuity. The structured grid uses less computational memory as compared to an unstructured grid [27]. Since the points are uniformly spaced, the solution with a structured grid converges better and has higher resolution. However, it is not always possible to represent complex geometries using a structured mesh.

Unstructured Grid

Unstructured meshes have irregular connectivity and incur a large memory storage. It needs explicit storage of neighborhood points and is usually comprised of triangular elements. The solution of an unstructured mesh may take more time to converge compared to the solutions of a structured mesh. In addition, the unstructured mesh may cause numerical instability or may not converge to the correct solution if care is not taken in maintaining the geometrical quality of the grids.

Hybrid Grid

The hybrid grid has the combination of structured and unstructured meshes in a efficient way. The meshing is first carried out with regular geometries where it is possible to generate a structured mesh and then the complex geometries are meshed in an unstructured manner. This can be conformal or non-conformal, which means that the grids from one part of the mesh may not intersect with those in the other regions [28]. A hybrid grid was employed to generate the mesh in the current work.

Grid generation was done using the Fluent™ mesher, the inbuilt mesh generation package. Figure 2.11 shows the hybrid mesh, which consists of a 98 percent structured hexagonal grid. The structured scheme in the grid aids in decreasing the computational time when compared to a totally unstructured grid which was initially attempted. Also, a grid independence study was made for three levels of meshing and the current sizing was chosen. It can be seen that the meshes are unstructured and denser in the vicinity of the inlet ports. The number and type of cell elements are shown in Table 2.10.

Figure 2.10. Mesh specifications.

Grid scheme	Number of Nodes	Number of Elements	Tetrahedral Cells	Wedges Cells	Pyramids Cells	Hexahedral Cells	Polyhedral Cells
Unstructured	9 550	44 817	44 817	0	0	0	0
Hybrid	127 255	119 808	2 040	0	368	117 400	0

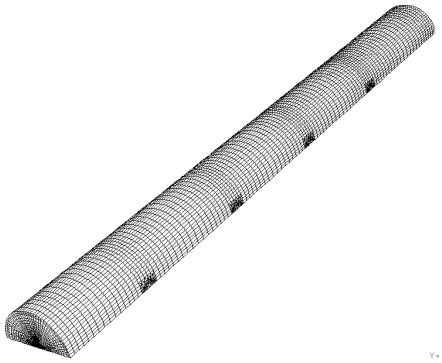

Figure 2.11. Isometric View of Mesh.

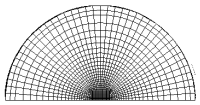

Figure 2.12. Front view of mesh.

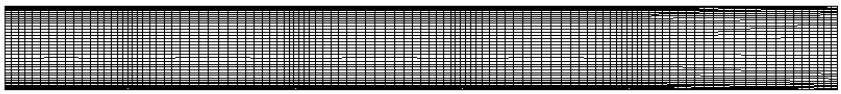

Figure 2.13. Top view of mesh.

Figure 2.14. Side view of mesh.

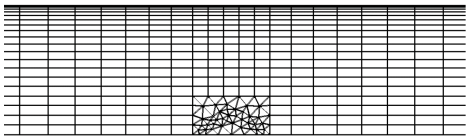

Figure 2.15. Detail view of the inlet port.

The grid is generated to encompass nine inlet ports, among which the eight side wall portions are manipulated to represent Cases 1–4. For representing Case 1 (Fig. 2.16), the side wall injections are considered as a wall boundary. In representing the other cases, the side wall injections are made normal to the boundary for Case 2 (Fig. 2.17), at an angle of 45° towards the exit for Case 3 (Fig. 2.18), at an angle of 45° towards the end wall for Case 4 (Fig. 2.19) and staggered side wall injection at an angle of 45° towards the end wall for Case 5 (Fig. 2.20).

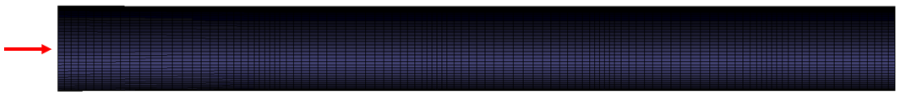

Figure 2.16. Case 1: endwall injection.

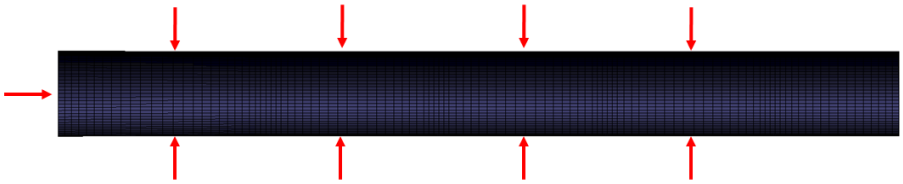

Figure 2.17. Case 2: normal sidewall injection..

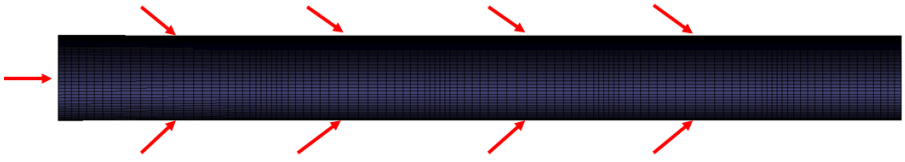

Figure 2.18. Case 3: inclined sidewall injection towards the downstream at 45°..

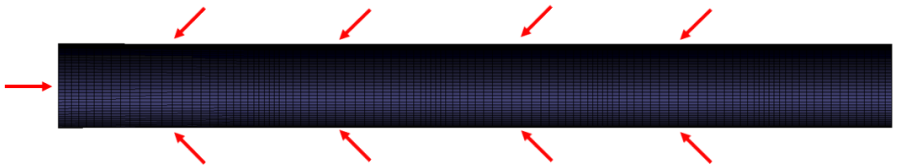

Figure 2.19. Case 4: inclined sidewall injection towards the upstream at 45°..

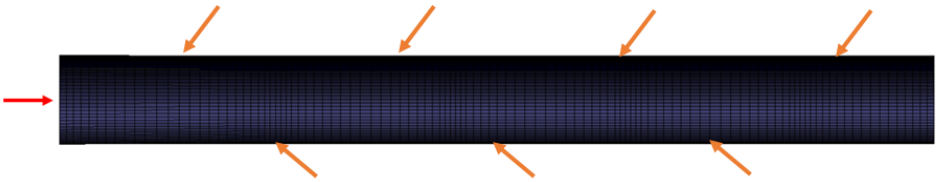

Figure 2.20. Case 5: staggered sidewall injection inclined towards the upstream at 45°..

2.5 Solver Settings

The background of the implicit formulations used to solve the flow equations were discussed in section 2.2.8 and the k–ε turbulence model was discussed in section 2.3. There are other factors with regard to the solver which have to be defined to obtain a stable and converged solution. A limited discussion is made on the theory of parameters with emphasis on the settings.

2.5.1 Relaxation Factor

The equations for mass, momentum and energy are solved iteratively using the implicit formulation. When there is a sudden or sharp change in the value of certain flow variables, the solver may either go unstable or not converge. In order to avoid this and reduce oscillations in the solution, a relaxation factor is used. It defines the

fraction of the value that has to be taken from the previous iteration to dampen the solution [29].

The relaxations usually make the solution converge slower, i.e., over a longer time. In the current work, initially, no relaxation factors were used to converge the solution faster (the values were set to unity). However, since the solution became unstable, relaxation factors were incorporated. The value of the relaxation factors for different variable are shown in Table 2.1.

Table 2.1. Relaxation factors.

Variable	**Pressure**	**Density**	**Body Forces**	**Momentum**	k	ε	μ_k
Relaxation Factor	0.45	1	1	0.75	0.9	0.9	1

2.5.2 Pressure–Velocity Coupling

Pressure–velocity coupling is done through a predictor-corrector method. The initial step, known as the "prediction" step, begins with a function fitted to functional values at a previous spatial location to predict (extrapolate) the values at each successive point using that function. The next "corrector" step refines the first approximation from the prediction step by using the predictor value and another method to interpolate the value at a same point [30].

Fluent™ supports different pressure–velocity coupling algorithms, namely, SIMPLE, SIMPLER, PISO and FSM. The coupling algorithm used for the current research is SIMPLE. SIMPLE stands for Semi Implicit Method for Pressure Linked Equations and more details can be found in almost all books on computational fluid dynamics and also in the orginal work of Patankar [31]. Table 2.2 lists the spatial discretization schemes.

Table 2.2. Spatial discretization

Variable	**Scheme**
Pressure	PRESTO
Momentum	Second Order Upwind
Volume Fraction	Modified HRIC
Turbulent Kinetic Energy	Second-Order Upwind
Turbulent Dissipation Energy	Second-Order Upwind

2.5.3 Input Parameters

The input parameters that are required to be varied in the simulation are the geometries of the domain, velocity of the inlet, the fuel–air mixture and injection scheme. Table 2.3 shows the various input parameters and the total number of simulations involved in the current work. Owing to the large number of cases to be simulated and also the implicit scheme being adopted, the solution on a desktop workstation becomes obsolete and impossible to simulate the vast number of cases. Therefore the simulations were carried out in two computing facilities, namely, HPC and the TACC, which provided enormous computational resource required for the current work.

Table 2.3. Input Parameters

Variable	Parameter	Cases
Fill geometries	Cases 1–5	5 (for simultaneous) 4 (for phased)
Velocity	50–200 m/s in steps of 25 m/s	7
Fuel–air mixture	Hydrogen–air Methane–air Propane–air Octane–air Biogas–air	5
Injection Scheme	Simultaneous Phased	2
	Total No. of cases	**315 cases.**

2.5.4 Injection scheme

In the configurations with sidewall ports, the reactants can either be injected simultaneously or can be injected in a phased manner. The injection velocities explored in the work are from 50–200 m/s in increments of 25 m/s. Phased injection was attempted for the same velocity range. Phased injection was expected to provide improvements in the fill time and was suggested in previous work [15]. The timing of the phased injection through the side wall ports require a thorough understanding of the fill fraction with time. Therefore, simultaneous injections were performed as the first step and the data of fill fraction with time was used to determine the sequence and timing for phased injection. This yielded more time of fill compared to simultaneous injection as the overall mass injected is less for phased injection.

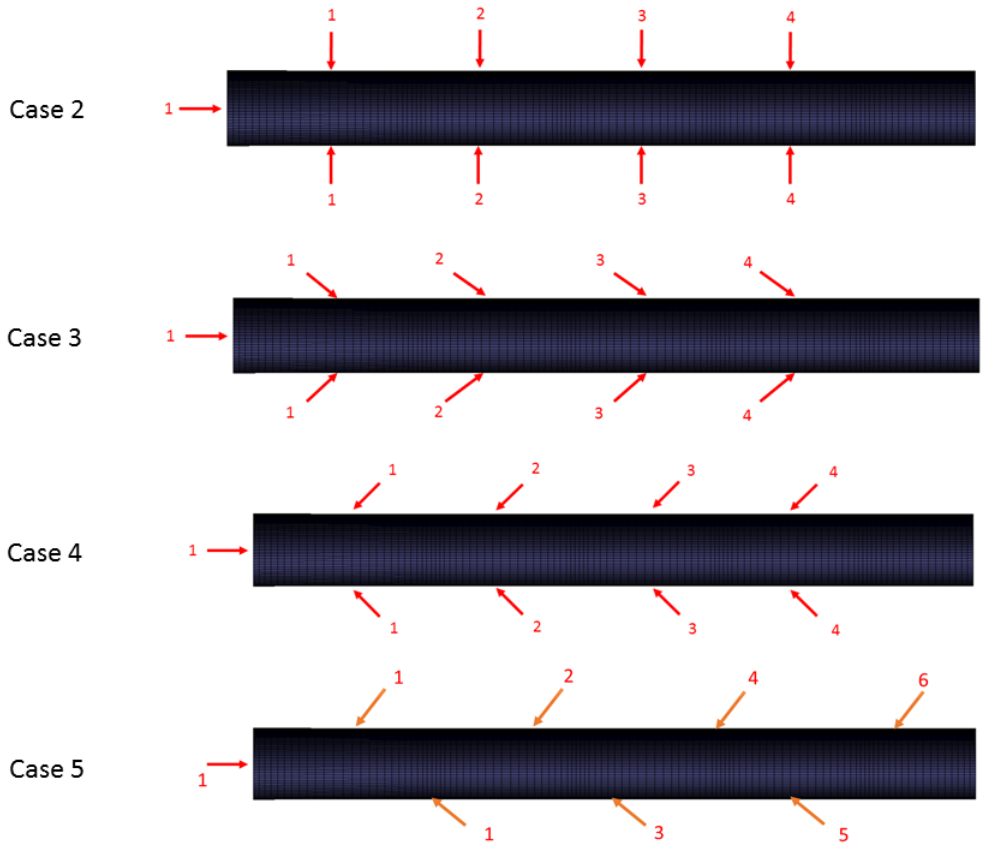

Figure 2.21. Schematic showing the terminology used for naming the ports in the phased injection scheme.

For the rapid fill configurations of Cases 2–4, the total tube length was divided into four sets and the time to fill each elemental part was calculated analytically based on the dimension of the part of tube considered. The first set of ports consists of the end wall and the nearest two side wall ports. These are followed by three pairs of side wall ports, namely, called "Port Set 2" and so forth (Fig. 2.21). For Case 5, the first set of inlet consists of end wall port along with two staggered ports. For all the cases, the first set of ports start injecting from the beginning of the simulation, that is, at $t = 0$. Then every consecutive port set starts injecting until 90 percent volume

fraction is achieved in the tube. None of the ports were shut during this process. Also, hydrogen–air mixture was used as a baseline to find the timing value and sequence of phased injection. Same timing and sequence was used for phased injection using other fuels. Also, in calculating the time of injection, the hydrogen–air mixture was used to find the values of phased injection timings. The same timings of the side wall ports was used for all the other fuel–air mixtures.

2.5.5 Computational Resources

The flow charts in Figs. 2.22 and 2.23 show the procesess involved in solving the problem remotely. The preprocessing stage remains the same for utilizing both the resources. However, remotely accessing and operating the computing resources are made in an entirely different manner. Reference was made to the user manual and documentation for the University of Texas at Arlington's HPC (High Performance Computing) [32] and TACC (Texas Advanced Computing Center) [33]. HPC was accessed through a secured shell (SSH) protocol and TACC was accessed through Windows Secure Copy (Winscp) protocol. Also, the input file for both the resources is based on the Fluent™ TUI (text user interface) [34]. The sample input file is shown in Appendix A.

Table 2.4. Phased injection timing for Case 2

	Port	V m/s						
	Set	50	75	100	125	150	175	200
Opening time, s	1	0.0000	0.0000	0.0000	0.0000	0.0000	0.0000	0.0000
	2	0.0600	0.0450	0.0300	0.0250	0.0200	0.0175	0.0150
	3	0.0825	0.0620	0.0415	0.0345	0.0275	0.0241	0.0208
	4	0.0975	0.0735	0.0495	0.0411	0.0328	0.0288	0.0248

Table 2.5. Phased injection timing for Case 3

	Port	V m/s						
	Set	50	75	100	125	150	175	200
Opening time, s	1	0.0000	0.0000	0.0000	0.0000	0.0000	0.0000	0.0000
	2	0.0650	0.0500	0.0350	0.0281	0.0213	0.0189	0.0165
	3	0.0890	0.0683	0.0475	0.0386	0.0298	0.0264	0.0230
	4	0.1050	0.0808	0.0565	0.0461	0.0358	0.0316	0.0275

Table 2.6. Phased injection timing for Case 4

	Port	V m/s						
	Set	50	75	100	125	150	175	200
Opening time, s	1	0.0000	0.0000	0.0000	0.0000	0.0000	0.0000	0.0000
	2	0.0575	0.0425	0.0275	0.0231	0.0188	0.0169	0.0150
	3	0.0825	0.0618	0.0410	0.0345	0.0280	0.0248	0.0215
	4	0.0975	0.0738	0.0500	0.0429	0.0358	0.0309	0.0260

Table 2.7. Phased injection timing for Case 5

	Port	V m/s						
	Set	50	75	100	125	150	175	200
Opening time, s	1	0.0000	0.0000	0.0000	0.0000	0.0000	0.0000	0.0000
	2	0.0500	0.0425	0.0350	0.0250	0.0150	0.0150	0.0150
	3	0.0630	0.0523	0.0415	0.0310	0.0205	0.0196	0.0188
	4	0.0750	0.0610	0.0470	0.0368	0.0265	0.0244	0.0223
	5	0.0870	0.0698	0.0525	0.0424	0.0323	0.0288	0.0253
	6	0.0985	0.0783	0.0580	0.0479	0.0378	0.0329	0.0280

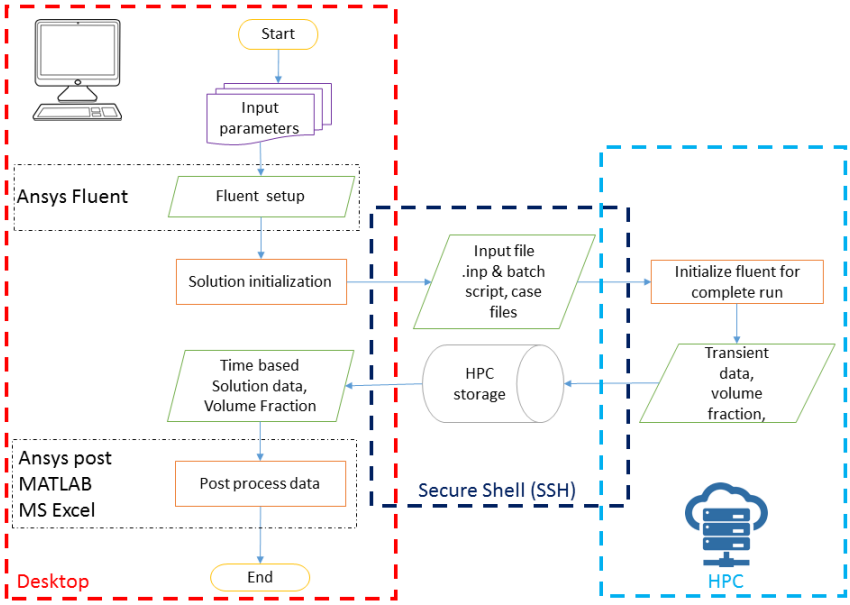

Figure 2.22. Processes involved in accessing HPC.

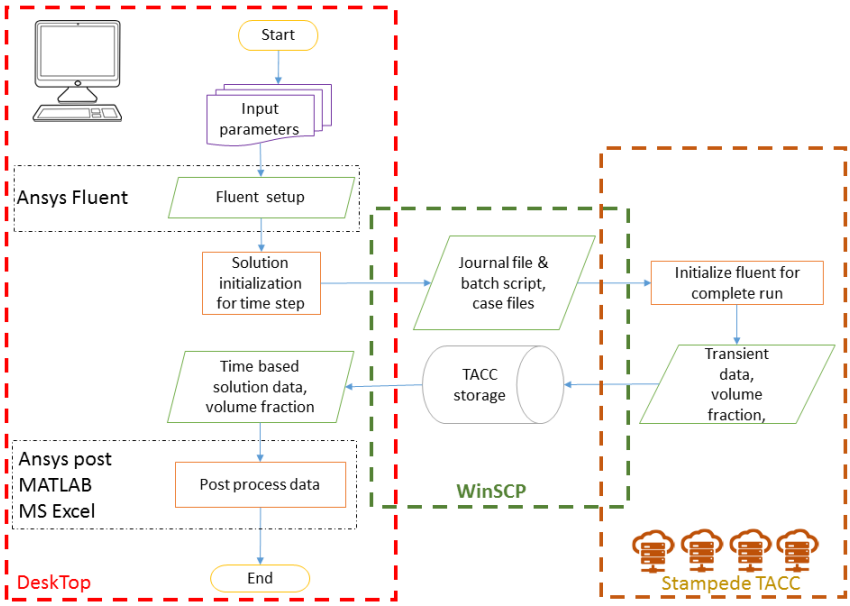

Figure 2.23. Processes involved in accessing TACC.

2.6 Convergence

Convergence is an essential criterion for establishing a stable and accurate solution. The convergence of the present case can be quantified by using the residual values at each iteration. The Fluent™ technical manual suggests the RMS values of residuals for each variable to be in the range 10^{-4}–10^{-5} for a well-converged solution in implicit multiphase problems [35]. The residuals for a typical run using a hybrid mesh is shown in Fig. 2.24. The peaks show the successive time steps in an implicit time-marching scheme. This is due to the change in the value of variable at every consecutive iteration. The figure shows that convergence was achieved.

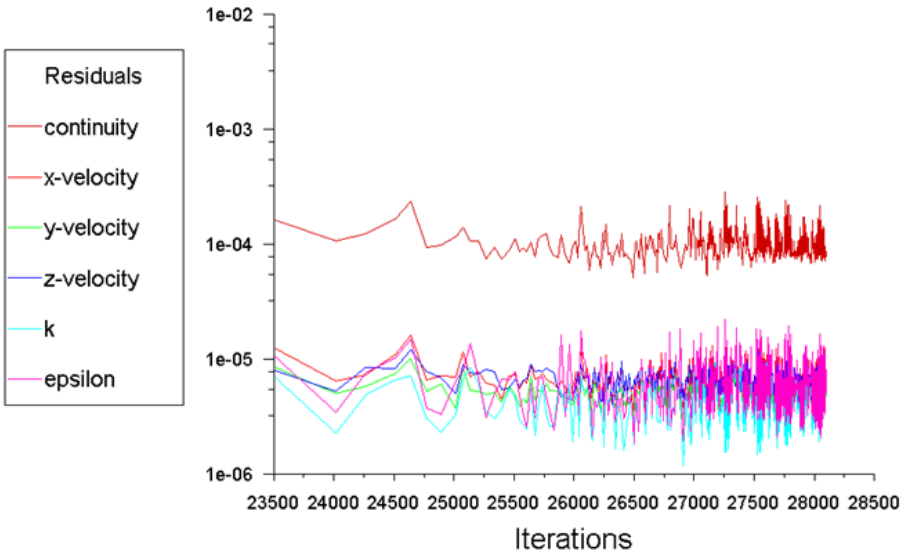

Figure 2.24. Plot showing the residual for a run using a hybrid mesh.

CHAPTER 3

Results and Discussion

The results are post-processed using ANSYS™ CFD-Post which offers flexibility in loading transient results in a single case. In doing so, it is easy to infer time-dependent results. The post-processing required a robust platform to load the results and often involved a large amount of time and storage.

The overall data processing approach can be described as follows. It involved monitoring the volume fraction of the domain, with the data saved for every five time steps. This roughly accounted to 250 raw data files. These data files were then post-processed and displayed, as discussed in §3.3. The parameters of interest are now discussed.

3.1 Transient Volume Fraction

Transient fill fraction data ϕ were helpful to infer the rapidity that the detonation tube was filled for the different port configurations. Due to the large number of cases studied, only selected examples of different fuel–air compositions are displayed to illustrate the effect of injection speed and port configurations.

3.1.1 Case 1

A plot of the rate at which the volume of the detonation tube being filled with a hydrogen–air mixture is shown in Fig. 3.1. The figure shows that filling is rapid until approximately 82 percent of the volume, after which the rate of fill decreases.

The figure also indicates the time required to achieve 70, 80 and 90 percent fill to be 118, 142 and 245 ms respectively.

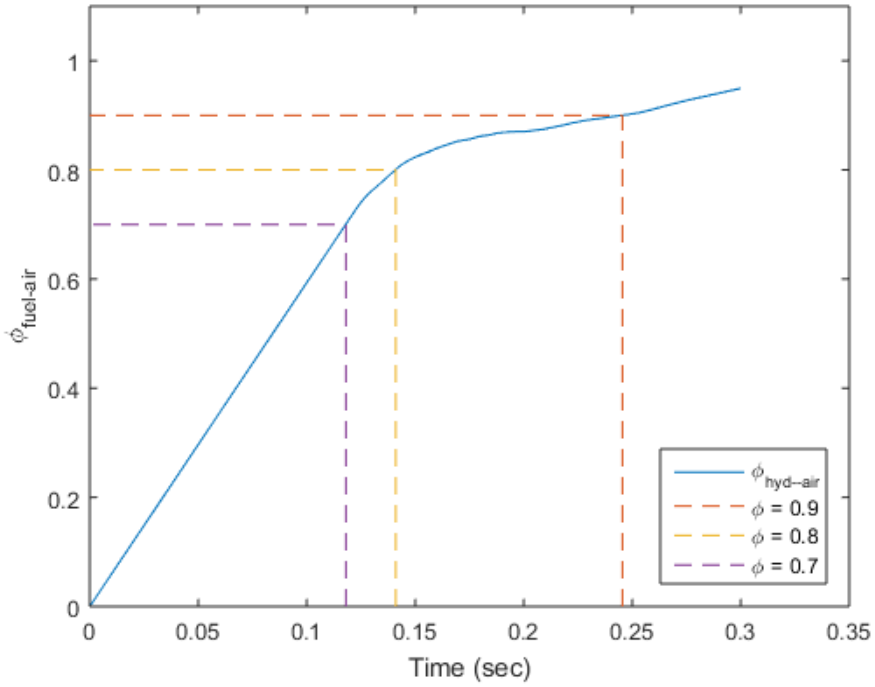

Figure 3.1. Rate of fill for hydrogen–air at 150 m/s for Case 1.

3.1.2 Case 2

With a larger number of ports, Case 2 is expected to fill the detonation tube more rapidly than Case 1 which proves to be true. Figure 3.2 shows both simultaneous and phased filling of a stoichiometric propane–air mixture injected at 150 m/s in solid blue and red lines respectively. For the simultaneous fill situation, a 90 percent fill is achieved in 42 ms compared to 245 ms for Case 1, albeit the illustration described above was with a stoichiometric hydrogen–air mixture. It can be noted that the 70 and 80 percent fill times are 19.2 and 26.3 ms. In particular, from 70 to 90 percent fill required a doubling in time. This indicates that while Case 2 is able to decrease the

fill time drastically through mass flow increase it is not really helpful in scavenging out the dead air effectively. Phased filling in this configuration started to fill the tube slowly but was able to reduce the fill time from 42 to 36 ms, showing some benefit.

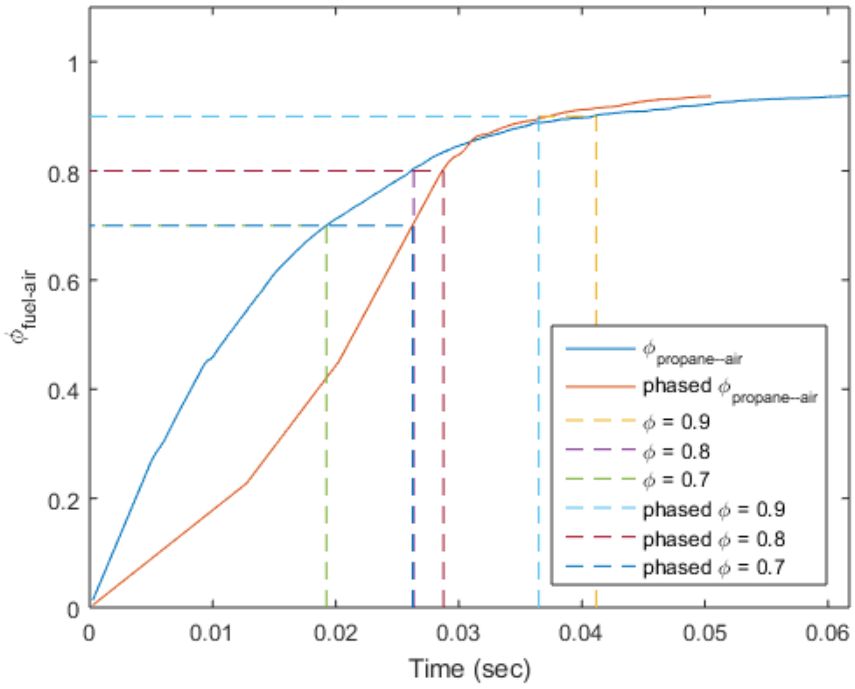

Figure 3.2. Rate of fill for propane–air at 150 m/s for Case 2 for both simultaneous and phased fill.

3.1.3 Case 3

Likewise, Fig. 3.3 combines the simultaneous and phased fill for Case 3 with methane–air at 150 m/s. However, unlike Case 2, this configuration required an excessive fill time despite having a large number of ports. The 90 percent fill time t_{fill} for simultaneous fill is 97 ms compared to 41 ms for Case 2. Phased filling, as in Case 2, started filling the tube slowly. It was better than simultaneous filling and reduced the 90 percent fill time to 70 ms. The time required to reach 80 percent

fill for simultaneous filling is 42 ms and not much shorter for phased filling. Such a configuration cannot achieve high cycle frequency using the 90 percent fill criterion.

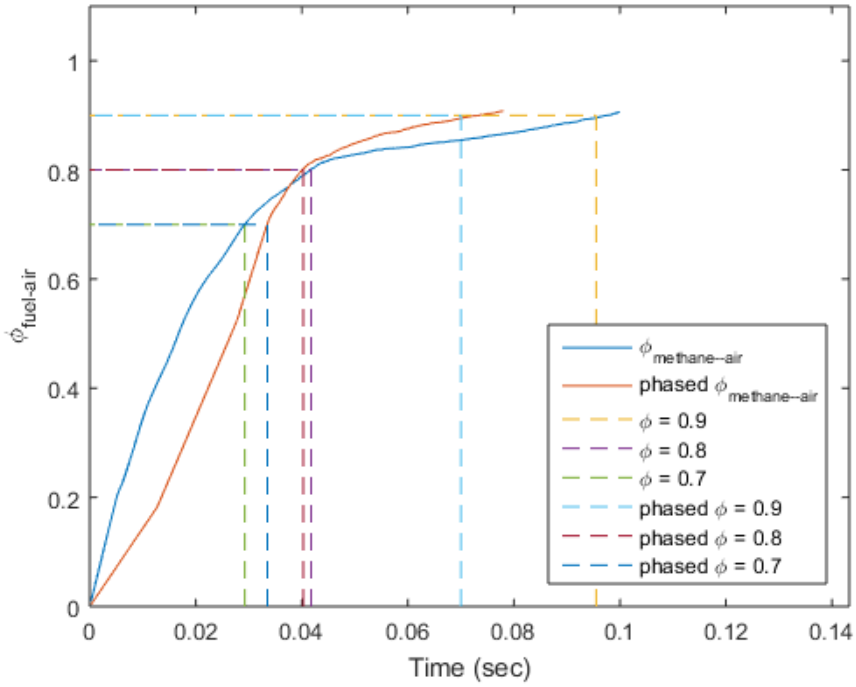

Figure 3.3. Rate of fill for methane–air at 150 m/s for Case 3 for both simultaneous and phased fill.

3.1.4 Case 4

Figure 3.4 is an example of simultaneous and phased fill with a stoichiometric, gaseous octane and air mixture. In this example, the filling time is comparable to Case 2. The times to achieve 80 and 90 percent fill are 32 and 44 ms respectively. For phased filling, the time to achieve 90 percent fill is 41 ms. Of note is that the time to reach 80 percent using phased fill is longer than for simultaneous fill. Given the short fill times, this configuration using either simultaneous or phased filling is suitable for rapidly filling a large detonation tube.

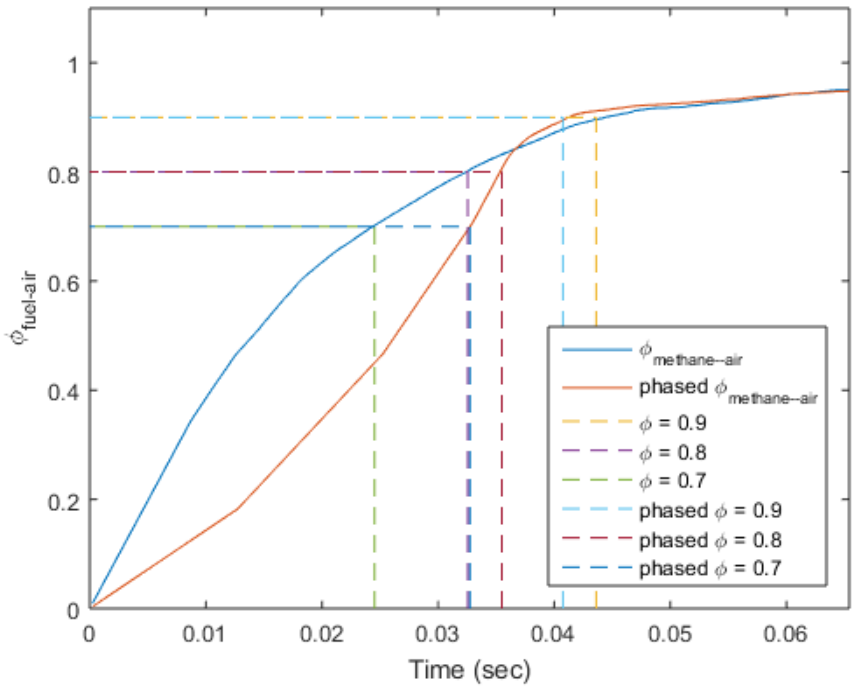

Figure 3.4. Rate of fill for octane–air at 150 m/s for Case 4 for both simultaneous and phased fill.

3.1.5 Case 5

Figure 3.4 shows the rate of fill for a biogas–air mixture through a staggered port configuration. The staggered configuration is perceived to yield a more uniform fill. However, in this configuration, geometrical constraints allowed only one end port and seven side ports to be utilized. This total of eight ports is one less than those in Cases 2–4. The time required to reach 90 percent fill is 56 ms. The figure shows that phased filling resulted in minimal improvement in filling time compared to simultaneous fill.

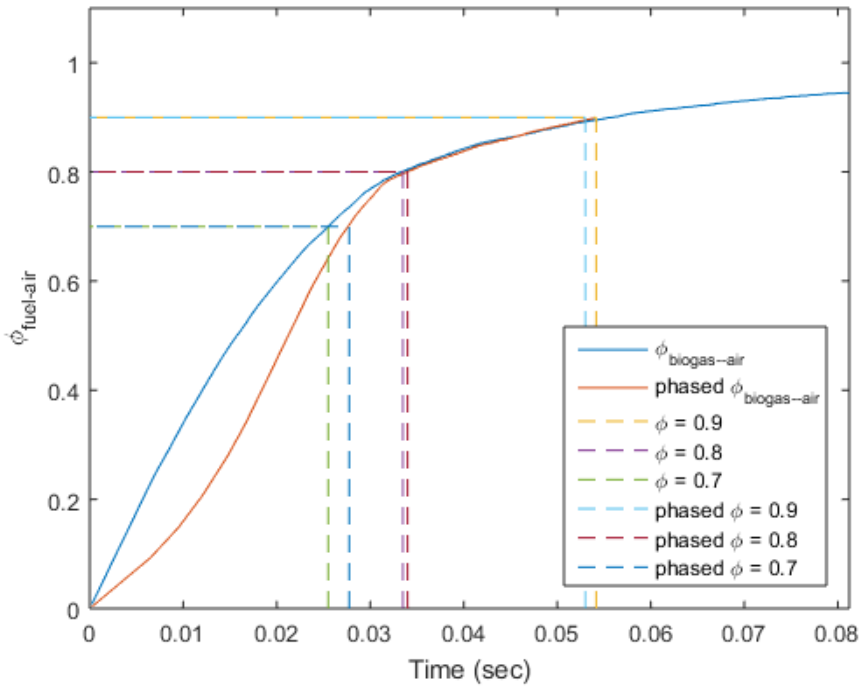

Figure 3.5. Rate of fill for biogas–air at 150 m/s for Case 5 for both simultaneous and phased fill.

3.2 Time of Fill

The large amount of data was organized using box plots. The box plot is one of the most widely used ways of representing the distribution of data with five elements. The minimum and maximum values form the upper- and lowermost lines, the median is the center line on the box and the center rectangle is bound by the first and third quartile of the distribution. This provides an easy way to compare the cases and the effect of reactants in an easy-to-comprehend manner. A discussion on individual cases is provided below.

3.2.1 Case 1

The end-wall configuration fill profile was discussed in §3.1.1. As a further extension, Fig. 3.6 shows the variation of fill time t_{fill} with velocities of injection from 50–200 m/s for different fuels. From Table 3.1, it can be observed that the minimum t_{fill} occurs for hydrogen at 200 m/s corresponding to 200 ms. This is too long as low as it leads to a cycle frequency of 2.5 Hz based on Eqn. (1.5). The maximum t_{fill} of 992 ms occurs for a propane–air mixture at 50 m/s, which leads to a cycle frequency of only 0.5 Hz. Therefore, end-wall filling of a large detonation tube will not be able to satisfy the cycle frequency requirement of a practical PDE.

Table 3.1. Fill time of different fuel–air mixtures with injection velocity of 50–200 m/s for Case 1

V	Fill time, s				
m/s	hyd–air	prop–air	oct–air	met–air	bio–air
50	0.793	0.993	0.924	0.950	0.956
75	0.553	0.663	0.625	0.626	0.630
100	0.395	0.503	0.481	0.466	0.471
125	0.298	0.398	0.379	0.372	0.374
150	0.245	0.325	0.312	0.304	0.305
175	0.218	0.284	0.273	0.264	0.265
200	0.200	0.252	0.240	0.233	0.234

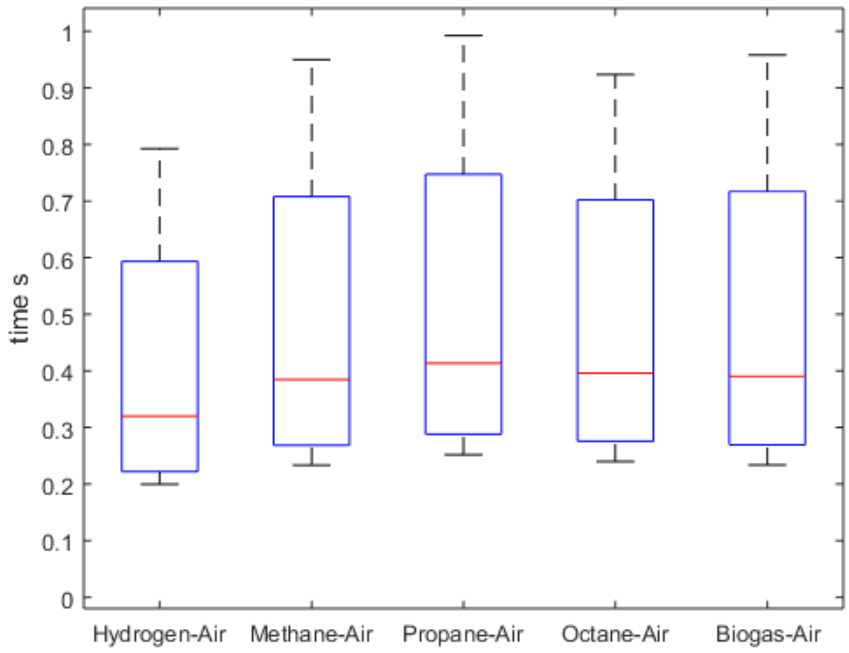

Figure 3.6. Fill time of fuel–air mixtures with injection velocity of 50–200 m/s for Case 1.

3.2.2 Case 2

A similar box plot as for Case 1 is shown in the Fig. 3.6 for the velocity ranges from 50-200 m/s and for different fuels, as well as for simultaneous and phased injection. From Table 3.2, the minimum t_{fill} occurs for methane–air and hydrogen–air mixtures at 200 m/s corresponding to 28 ms. Based on Eqn. 1.5, this yields a cycle frequency of 18.5 Hz. This is comparatively higher than the end wall configuration but is not sufficiently high for aerospace requirements. Phased injection, as discussed previously for the specific injection velocity of 150 m/s but which is generally valid, shows a reduction in fill time compared to simultaneous injection. The minimum fill time for phased injection occurs for a methane–air mixture at 200 m/s injection velocity. This is a marginal reduction and is also observed for all fuel–air combinations.

Table 3.2. Fill time of simultaneous injection of different fuel–air mixtures with injection velocity of 50–200 m/s for Case 2

V	Fill time, s				
m/s	hyd–air	prop–air	oct–air	met–air	bio–air
50	0.112	0.129	0.123	0.110	0.116
75	0.0744	0.0853	0.0817	0.0729	0.0775
100	0.0559	0.0639	0.0607	0.0545	0.0581
125	0.0447	0.0512	0.0487	0.0438	0.0466
150	0.0373	0.0422	0.0405	0.0365	0.0388
175	0.0320	0.0365	0.0346	0.0313	0.0333
200	0.0280	0.0323	0.0303	0.0275	0.0292

Table 3.3. Fill time of phased injection of different fuel–air mixtures with injection velocity of 50–200 m/s for Case 2

V	Fill time, s				
m/s	hyd–air	prop–air	oct–air	met–air	bio–air
50	0.0988	0.112	0.110	0.0951	0.101
75	0.0646	0.0756	0.0709	0.0646	0.0673
100	0.0485	0.0566	0.0527	0.0478	0.0515
125	0.0392	0.0453	0.0427	0.0381	0.0404
150	0.0324	0.0370	0.0352	0.0317	0.0337
175	0.0280	0.0320	0.0307	0.0278	0.0292
200	0.0246	0.0286	0.0266	0.0244	0.0258

3.2.3 Case 3

Figure 3.8 presents box plots for simultaneous and phased injection for Case 3 which consists of an endwall port and sidewall ports pointed at 45° downstream. From Table 3.4, the minimum t_{fill} for this configuration occurs for a hydrogen–air mixture at 200 m/s corresponding to 62.8 ms. This gives a cycle frequency of 8 Hz which is extremely low. The maximum t_{fill} for this configuration is 220 ms for a propane–air mixture at 50 m/s. A very low cycle frequency of 2.3 Hz is achieved.

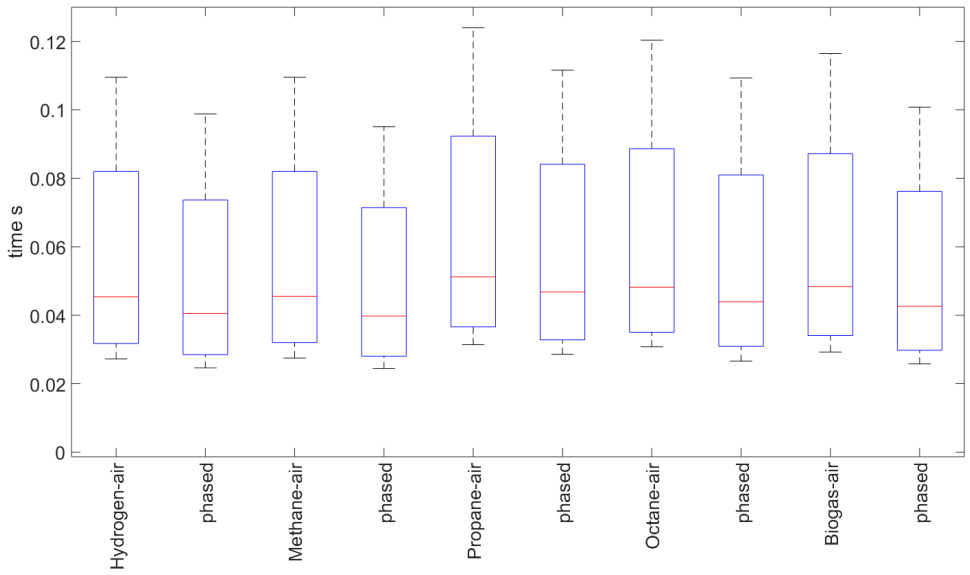

Figure 3.7. Fill time of fuel–air mixtures with simultaneous and phased injection for Case 2.

Therefore using this configuration as a means of decreasing the t_{fill} does not appear to be feasible. The long fill time for all the mixtures in Case 3 may be due to the fact that injecting the flow at 45° would have essentially convected more of the material downstream instead of assessing the upstream as well. Further discussion will be provided in §3.4.

Phased injection for Case 3 yields a dramatic reduction in fill time, as can be seen in Fig. 3.8 and Table 3.5. With phased injection, the minimum t_{fill} is 46 ms for the hydrogen-air mixture at an injection velocity of 200 m/s. Unfortunately, though the fill time has been decreased, the operation frequency is still low.

3.2.4 Case 4

Figure 3.9 shows t_{fill} for simultaneous and phased injection with sidewall injectors inclined at 45° towards the upstream. From Table 3.6, the minimum t_{fill} for

Table 3.4. Fill time of simultaneous injection of different fuel–air mixtures with injection velocity of 50–200 m/s for Case 3

V	Fill time, s				
m/s	hyd–air	prop–air	oct–air	met–air	bio–air
50	0.193	0.220	0.213	0.193	0.205
75	0.158	0.180	0.173	0.167	0.177
100	0.128	0.146	0.138	0.148	0.156
125	0.104	0.118	0.113	0.121	0.127
150	0.0848	0.0968	0.0949	0.0968	0.1014
175	0.0711	0.0815	0.0786	0.0850	0.0896
200	0.0628	0.0723	0.0702	0.0730	0.0771

Table 3.5. Fill time of phased injection of different fuel–air mixtures with injection velocity of 50–200 m/s for Case 3

V	Fill time, s				
m/s	hyd–air	prop–air	oct–air	met–air	bio–air
50	0.140	0.162	0.155	0.141	0.150
75	0.116	0.130	0.125	0.120	0.130
100	0.0922	0.105	0.0990	0.1062	0.115
125	0.0747	0.0861	0.0814	0.0876	0.0936
150	0.0616	0.0697	0.0683	0.0700	0.0745
175	0.0522	0.0587	0.0571	0.0624	0.0645
200	0.0456	0.0521	0.0505	0.0531	0.0555

the configuration is 31 ms for the hydrogen–air mixture at 200 m/s, yielding a cycle frequency of 16 Hz. This frequency is better than Case 3 but less than Case 2. This configuration is thought to provide good fill uniformity compared to Cases 2 and 3 which will be discussed further in section 3.4. The maximum t_{fill} is 140 ms for a propane–air mixture at 50 m/s. Only a very low operational frequency of 3.6 Hz is achieved.

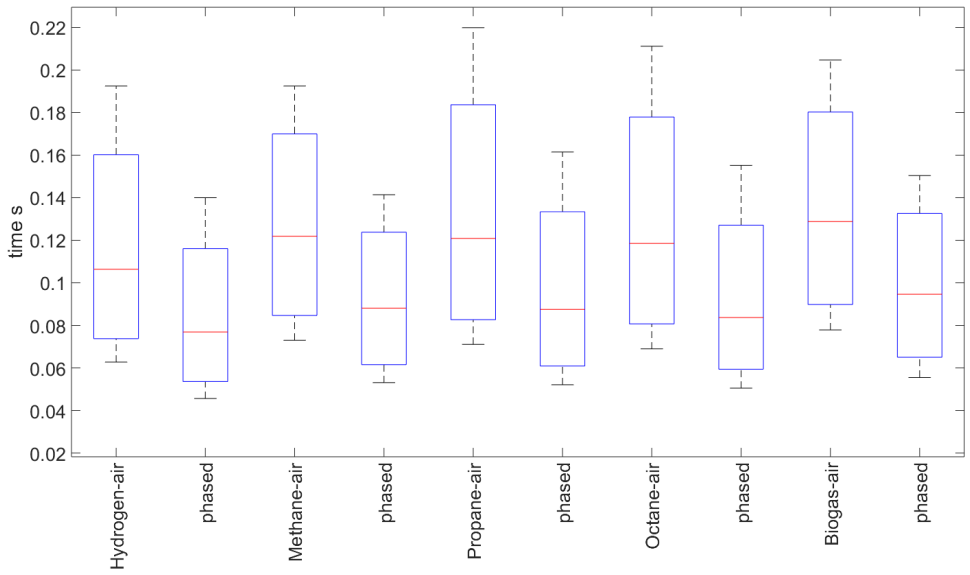

Figure 3.8. Fill time of fuel–air mixtures with simultaneous and phased injection for Case 3.

Phased injection data in Fig. 3.9 and Table 3.7 do not show significant reduction in fill time compared to simultaneous injection. With phased injection, the minimum t_{fill} is 29 ms which occurs for the hydrogen–air mixture at 200 m/s injection velocity. Notably, this configuration has fill times close to those of Case 2 which has the least fill time. Therefore, based on other metrics of filling such as spillage, fill uniformity and complexities involved in making angled ports, a choice can be made between Case 2 and Case 4.

Table 3.6. Fill time of simultaneous injection of different fuel–air mixtures with injection velocity of 50–200 m/s for Case 4

V	Fill time, s				
m/s	hyd–air	prop–air	oct–air	met–air	bio–air
50	0.126	0.140	0.134	0.128	0.136
75	0.0858	0.0963	0.0935	0.0877	0.0932
100	0.0615	0.0696	0.0676	0.0630	0.0670
125	0.0481	0.0550	0.0526	0.0493	0.0524
150	0.0414	0.0474	0.0446	0.0425	0.0452
175	0.0371	0.0426	0.0400	0.0378	0.0401
200	0.0310	0.0351	0.0344	0.0315	0.0335

Table 3.7. Fill time of phased injection of different fuel–air mixtures with injection velocity of 50–200 m/s for Case 4

V	Fill time, s				
m/s	hyd–air	prop–air	oct–air	met–air	bio–air
50	0.115	0.129	0.123	0.117	0.124
75	0.0786	0.0900	0.0865	0.0804	0.0871
100	0.0569	0.0638	0.0625	0.0583	0.0626
125	0.0449	0.0509	0.0492	0.0452	0.0485
150	0.0387	0.0443	0.0413	0.0397	0.0422
175	0.0347	0.0394	0.0366	0.0353	0.0368
200	0.0290	0.0321	0.0315	0.0294	0.0310

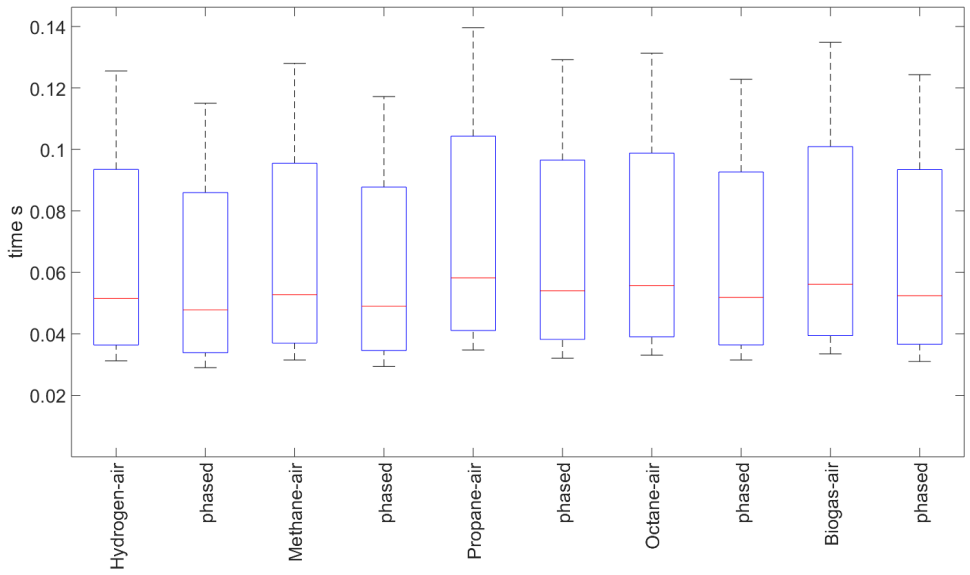

Figure 3.9. Fill time of fuel–air mixtures with simultaneous and phased injection for Case 4.

3.2.5 Case 5

Figure 3.10 shows t_{fill} for staggered side wall injectors inclined at 45° towards the upstream. This configuration gave similar t_{fill} values at high velocities irrespective of fuel, which can be inferred from the lower line in the box plot. As in the other cases, the minimum t_{fill} for the configuration is for the hydrogen–air mixture with a value of 37.5 ms, yielding a cycle frequency of 13 Hz. Note that the short t_{fill} time was achieved with eight ports instead of nine for the other rapid fill configurations. Unlike the minimum t_{fill}, the maximum time of fill shows a more obvious variation depending on the fuel–air mixture. The maximum t_{fill} is 174 ms for the propane–air mixture at 50 m/s. This corresponds to a low cycle frequency of 2.84 Hz. Only a small reduction in fill time is achieved with phased injection. For example, the minimum

t_{fill} is 36 ms for the hydrogen–air mixture at 200 m/s injection velocity. This time is more than the Case 2 and Case 4 configurations, but less than that of Case 3.

Table 3.8. Fill time of simultaneous injection of different fuel–air mixtures with injection velocity of 50–200 m/s for Case 5

V	Fill time, s				
m/s	hyd–air	prop–air	oct–air	met–air	bio–air
50	0.154	0.174	0.170	0.157	0.166
75	0.102	0.114	0.112	0.105	0.111
100	0.0750	0.0834	0.0810	0.0785	0.0832
125	0.0605	0.0684	0.0660	0.0630	0.0667
150	0.0508	0.0575	0.0558	0.0530	0.0562
175	0.0430	0.0487	0.0468	0.0451	0.0476
200	0.0375	0.0428	0.0407	0.0393	0.0413

Table 3.9. Fill time of phased injection of different fuel–air mixtures with injection velocity of 50–200 m/s for Case 5

V	Fill time, s				
m/s	hyd–air	prop–air	oct–air	met–air	bio–air
50	0.148	0.167	0.162	0.151	0.162
75	0.0975	0.111	0.108	0.1018	0.107
100	0.0721	0.0794	0.0778	0.0755	0.080
125	0.0587	0.0657	0.0635	0.0600	0.0647
150	0.0488	0.0552	0.0541	0.0504	0.0540
175	0.0413	0.0464	0.0445	0.0433	0.0453
200	0.0360	0.0408	0.0387	0.0381	0.0393

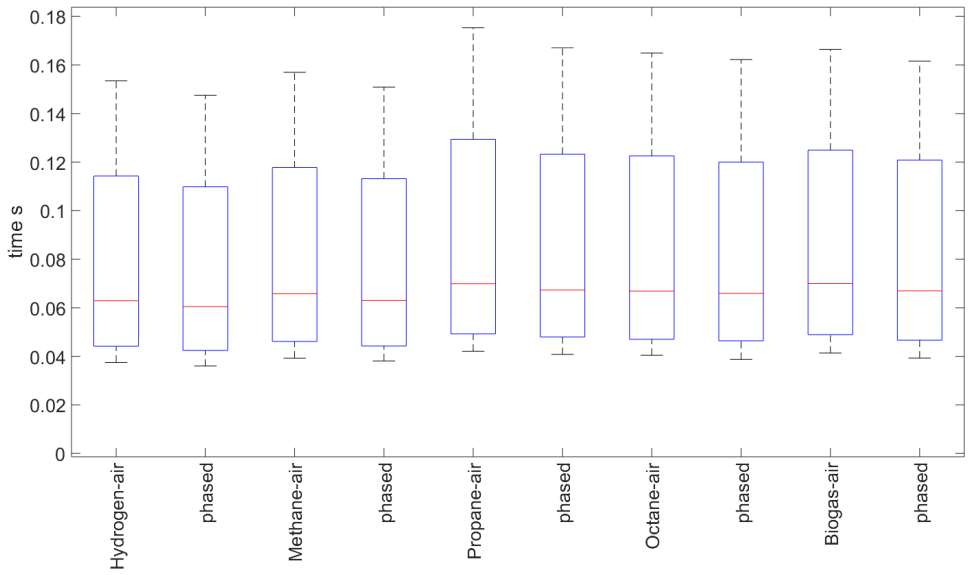

Figure 3.10. Fill time of fuel–air mixtures with simultaneous and phased injection for Case 5.

3.3 Quality of Fill

When the reactants are injected into the detonation tube, they displace the existing air in a nonuniform way. This nonuniform reactant distribution can have an adverse effect on detonation wave formation and propagation, even if the reactant mixture is uniform. Fill uniformity is difficult to determine experimentally but the features can be investigated numerically by carefully post-processing the data. A streamwise plot of volume fraction is obtained by "volume sweep" and the procedure is outlined below.

3.3.1 Volume Sweep

Consider the criterion that the time to fill the detonation tube t_{fill} is when the volume fraction reaches 90 percent. (The volume fraction at each cell in the entire

domain is obtained from CFD post at t_{fill}.) However, this 90 percent distribution is itself not uniform, varying throughout the tube from a minimum value of 0 which is void of the fuel–air phase and a maximum value of 1, which means that the cell is filled with only the fuel–air phase.

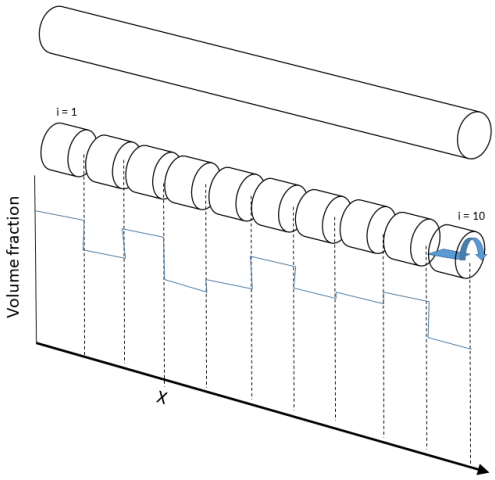

Figure 3.11. Schematic representation of volume sweep with ten elements.

Interpretation of the raw, three-dimensional data is faciliated by a one-dimensional representation as illustrated in Fig. 3.11 where the tube is divided into ten equal elements. The computational cells are assigned to the lengthwise elements by the centroid. Since the computational cells may cross the element boundaries, it was thought that assigning the cells to the elements is best done by locating the centroids. In general, the volume fraction of the ith element is given by summing the volume fractions of individual j cells within each i element as follows:

$$\phi_i = \frac{\sum_{j=1}^{n} \forall_{j,i} \phi_{j,i}}{\forall_i} \tag{3.1}$$

In the present implementation, the detonation tube is divided into $\{i : 1, 51\}$ segments of equal length. The values of j are variable and computed for each element, starting from 1 to n.

3.3.2 Case 1

Figure 3.12 shows that the volume fraction of the reactants along the tube at certain locatitons reaches values close to unity and exceeded 0.8 for about three-quarters of the tube. A one-to-one correspondence can be made with the contour plots shown in Fig. 3.13.

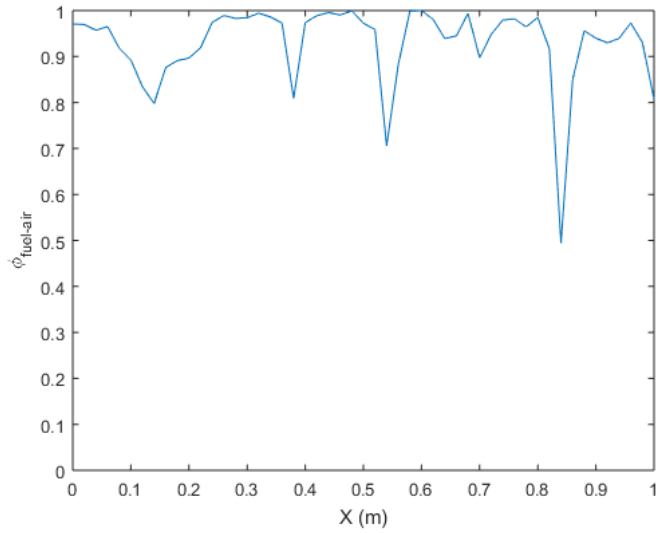

Figure 3.12. Case 1: streamwise distribution of ϕ at 245 ms.

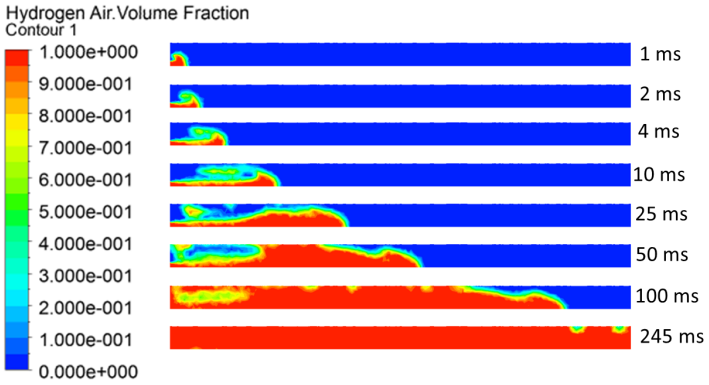

Figure 3.13. Case 1: hydrogen–air volume fraction at 150 m/s injection velocity.

3.3.3 Case 2

Figure 3.14 shows very low values of ϕ near the end wall up to nearly 0.2 m and ϕ value close to 0.8 until 0.4 m. This can be also seen in the contour plots in Figs. 3.15 and 3.16.

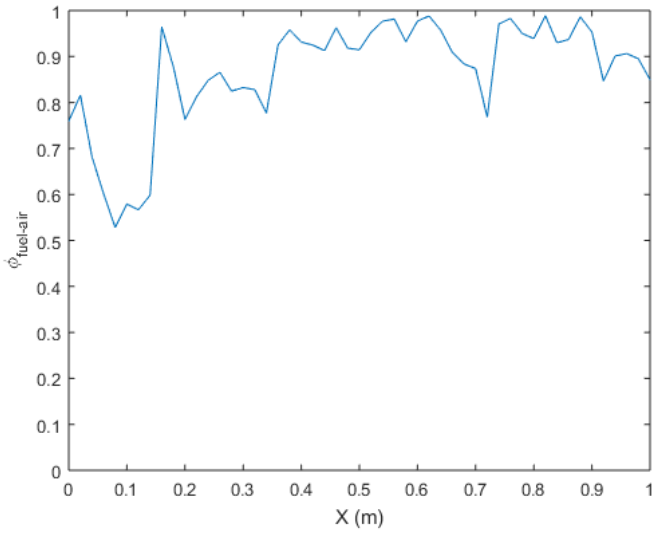

Figure 3.14. Case 2: streamwise distribution of $\phi_{methane-air}$.

The volume fraction contour on the mid-plane shows the pattern in which the reactant mixture impinges from the side-wall ports to produce a uniform fill. But the cross-sectional plane in Fig. 3.16 shows visible regions of dead-air near the end wall. This distribution may lead to difficulties in the DDT process since DDT enhancement devices, such as the Shchelkin spiral, are located in this region. This could be an area of investigation as many PDEs were able to demonstrate good performance with such filling configuration. This configuration has very good fill fraction after 0.4 m from the end wall and has the least t_{fill}.

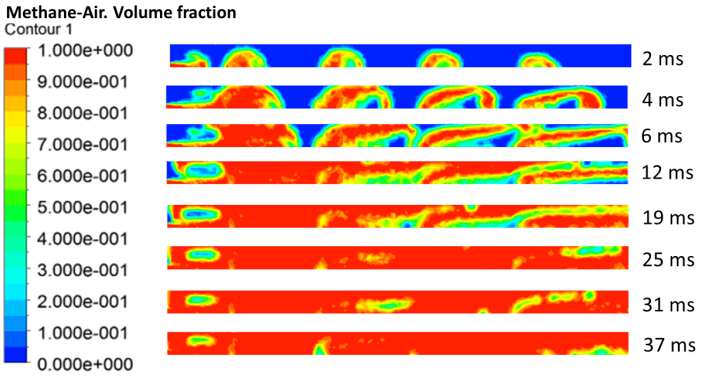

Figure 3.15. Case 2 methane-air volume fraction at mid-plane with 150 m/s injection velocity.

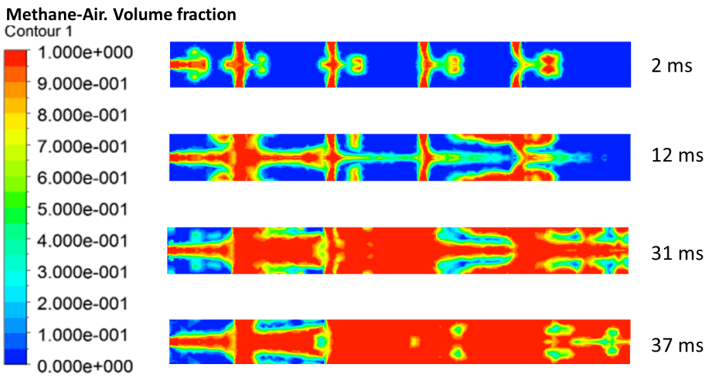

Figure 3.16. Case 2 methane-air volume fraction at cross section with 150 m/s injection velocity.

Figure 3.17 shows a low value of ϕ near the end wall for phased injection. The fill fraction until 0.4 m appears similar to the fill profile of simultaneous injection shown in Fig. 3.14. Examples of contour profiles of phased injection for Case 2 are shown in Figs. 3.18 and 3.19. The first two sidewall ports inject the reactant mixture 2 ms after the start of endwall injection. Subsequent pairs of ports open at 17 and 26 ms. At 31 ms, the chamber is filled with 90 percent $\phi_{methane-air}$ but the contour plots still show a dead air region near the end wall. Therefore, for fill uniformity, phased injection does not appear to yield an advantage over simultaneous injection, although there is a reduction of fill time by nearly 6 ms. Adopting phased injection at 150 m/s yields a cycle frequency of about 3 Hz.

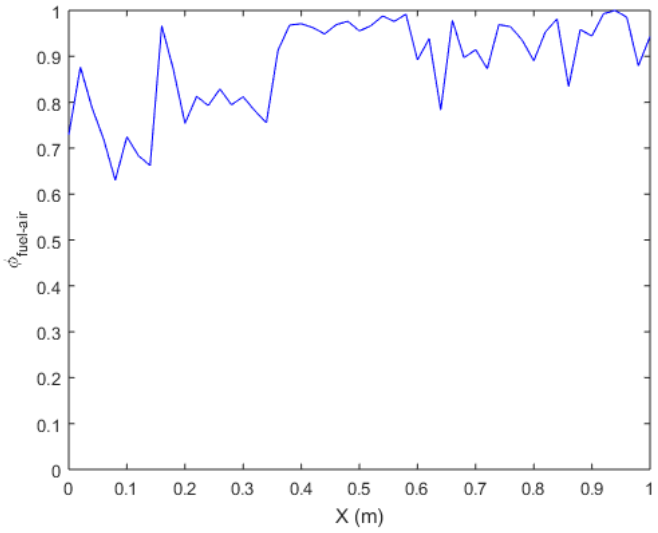

Figure 3.17. Case 2 with phased injection: $\phi_{methane-air}$ in streamwise direction.

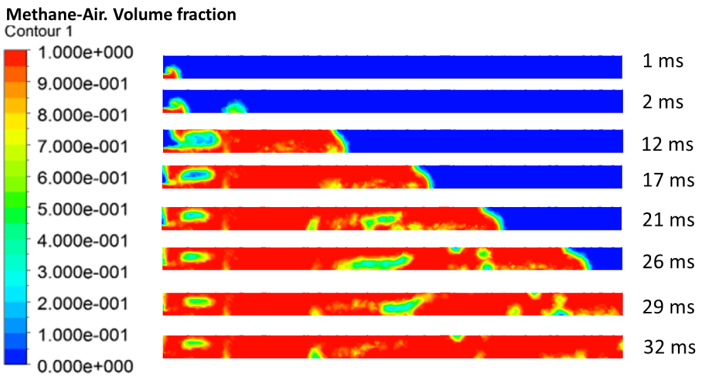

Figure 3.18. Case 2 methane-air volume fraction at mid-plane with 150 m/s phased injection velocity.

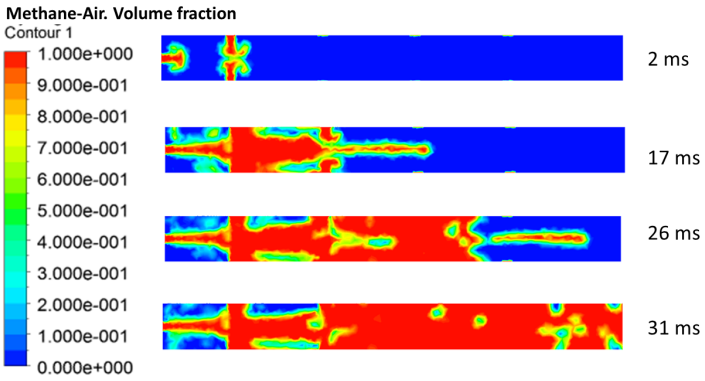

Figure 3.19. Case 2 methane-air volume fraction at cross section with 150 m/s phased injection velocity.

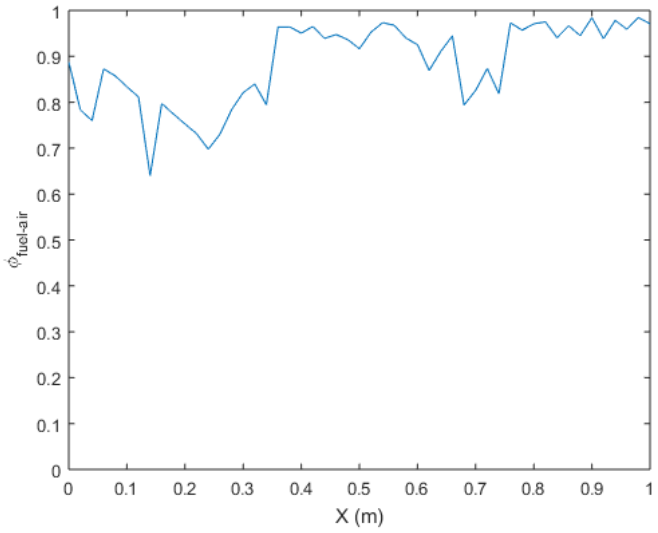

Figure 3.20. Case 3: streamwise distribution of $\phi_{propane-air}$.

3.3.4 Case 3

The plot of fill fraction in Figure 3.20 shows low values of ϕ near the end wall up to nearly 0.4 m, where the values of ϕ are close to 0.8 until 0.4 m. The contour plots in fig. 3.22 shows partial fill near exit at 75 ms.

The contour plots across the mid-plane as shown in Fig. 3.21 reveal a relatively uniform fill at later time, but as discussed in the above section, the cross-sectional contours show significant void regions up to 0.4 m even at later time. This configuration takes the longest time to fill compared to the other rapid fill configurations. The reason for this can be visualized in Fig. 3.22 which shows a steady stream of injected reactants being spilled out through exit. Thus, this configuration suffers from its inability to fill the dead-air region near the closed end and from the huge loss of reactant volume through the exit.

The filling profile for phased injection is shown in Fig. 3.23. The fill uniformity is poorer than simultaneous injection shown in Fig. 3.20. Also, there is a steady void

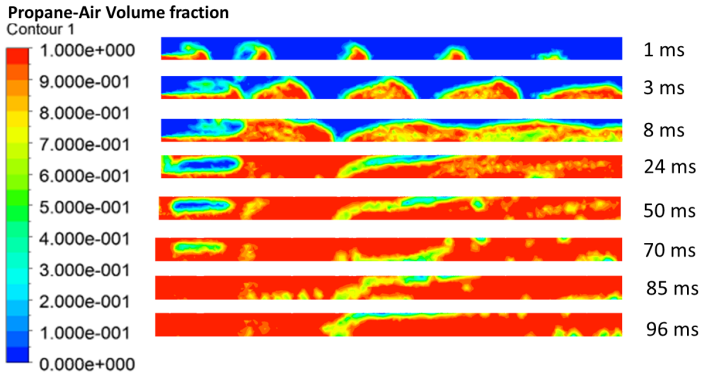

Figure 3.21. Case 3 propane-air volume fraction at mid-plane with 150 m/s injection velocity.

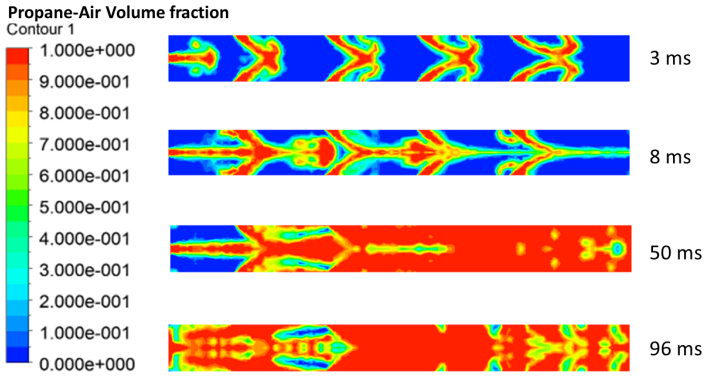

Figure 3.22. Case 3 propane-air volume fraction at cross section with 150 m/s injection velocity.

at 0.75 m from the end wall in the phased injection. Apart from the dead air region between 0.15 m and 0.4 m, there is a pockets of partially filled regions at 0.75 m with a fill ratio of 0.6 which is way lower than the expected fill fraction of 0.9, shown in 3.23.

Figure 3.24 and 3.25, shows that at 2 ms, the first two side-wall ports inject the methane–air mixture followed later at 15 ms and 47 ms by the subsequent pairs of sidewall ports. At 70 ms, the chamber is filled with 90 percent reactant. The contour plot reciprocates the fill profile that was observed through the volume sweep. There

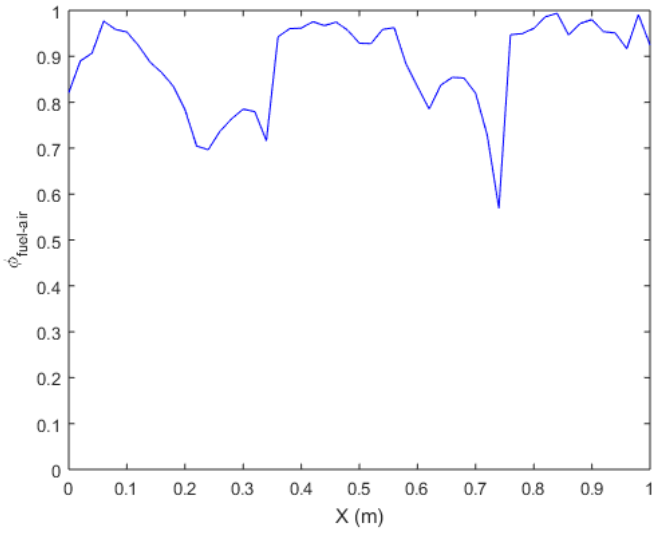

Figure 3.23. $\phi_{propane-air}$ in streamwise direction of Case 3 with phased injection using volume sweep.

is a steady dead air region near the walls from 0.2 m to 0.4 m and pockets of dead air near the exit of tube, which can be clearly inferred from Fig. 3.25 at 70 ms. Therefore, based on fill uniformity, phased injection has not made much of a contribution.

3.3.5 Case 4

Figure 3.26 which plots the streamwise fill fraction for a biogas–air mixture shows a relatively uniform fill fraction of 0.85–0.95 throughout the tube, except near the closed end. This configuration has a fill time comparable with Case 2. It is potentially a useful configuration for rapid fill, provided the fill near end wall is achieved. Further, the contour plots in Figures 3.27 and 3.28 show the dead air region being trapped within the small pocket near the end wall and along the sides at mid-section.

Figure 3.29 shows an example of the phased filling profile for biogas–air injected at 150 m/s. The filling profile is uniform for most part of the tube with a dip near

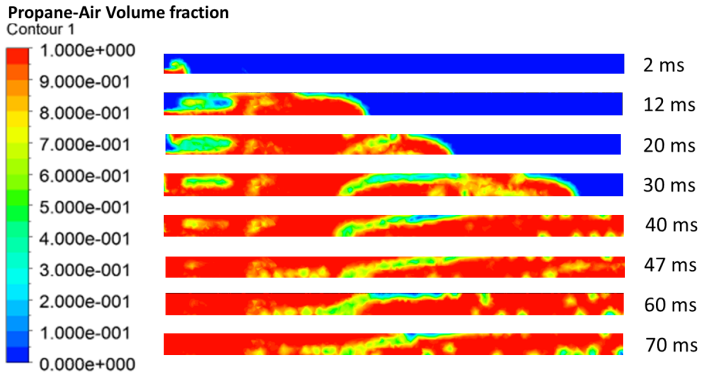

Figure 3.24. Case 3 propane-air volume fraction at mid-plane with 150 m/s phased injection velocity.

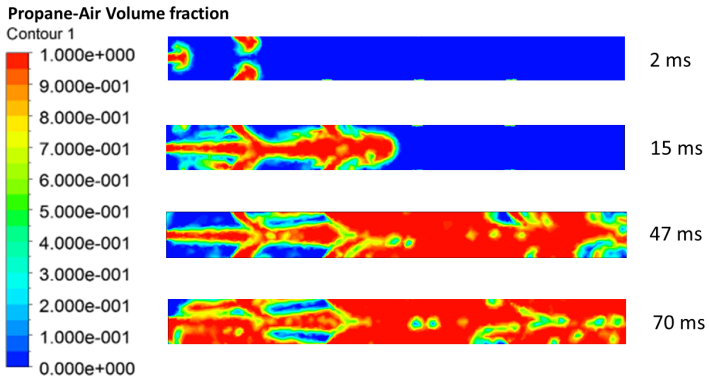

Figure 3.25. Case 3 propane-air volume fraction at cross section with 150 m/s phased injection velocity.

0.3 m from end wall but which is not less than 0.7. Therefore, the total fill quality is better than other rapid fill configurations.

Figure 3.30 and 3.31, shows that the first two side wall ports are turned on at 2 ms after the start of end wall injection. At 16 and 28 ms, the injection at the remaining two port pairs is made. At 42 ms, the chamber is filled with 90 percent of the reactants. The figure shows that phased injection has moved the void from near the end wall to a downstream location at 0.3 m.

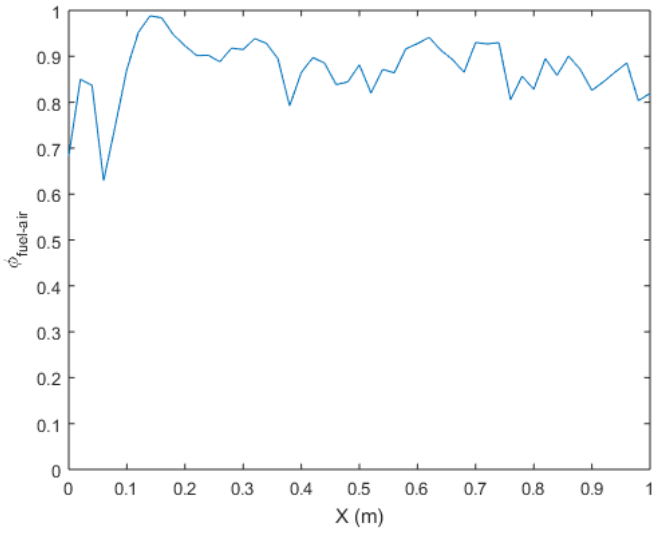

Figure 3.26. $\phi_{biogas-air}$ in streamwise direction for Case 4 using volume sweep.

3.3.6 Case 5

Figure 3.32 shows the fill fraction to be generally well above 0.8 except at 0.25 m from end wall. The region close to the end wall shows very good fill fraction of close to 0.95. This signifies the utility of the staggered configuration for achieving uniform fill rapidly.

The contour plots of Figs. 3.33 and 3.34 show complex flow patterns during the fill process. Generally, staggered injection yields a better fill profile except for a large void at around 0.25 m from the closed end. Also, the contour plots shows the fill fraction with the voids of dead air clearly at 53 ms in the fig. 3.34 between 0.65 m to 0.9 m.

Figure 3.35 shows the filling profile for phased filling. A large void is visible at 0.25 m from the end wall. The filling profile is relatively uniform with fill fraction of more than 0.85 for most part of the chamber except at that 0.25 m region. Also,

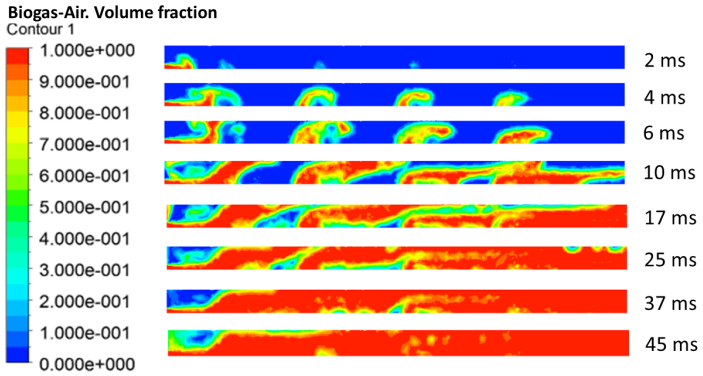

Figure 3.27. Case 4 biogas-air volume fraction at mid-plane with 150 m/s injection velocity.

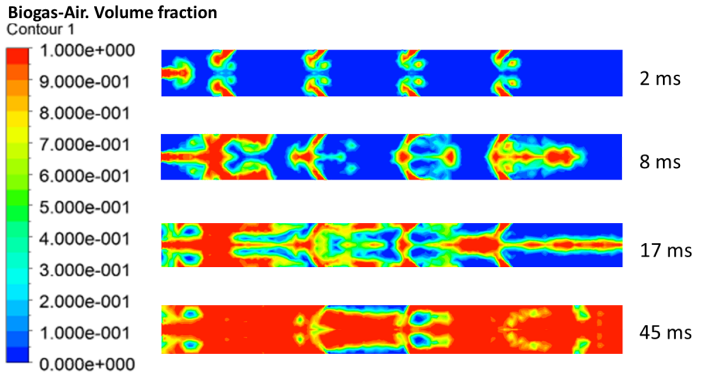

Figure 3.28. Case 4 biogas-air volume fraction at cross section with 150 m/s injection velocity.

There are two dead air region near the exit at 0.6 m and 0.9 m which can be visualized in the contour plot, shown in Figure 3.37 .

In Figure 3.37 and 3.36, we observe that at 2 ms the first two side-wall ports inject the octane–air mixture along with the end wall injection and, later, injection through each of the staggered ports are initiated. At 53 ms, the chamber is 90 percent filled with $\phi_{octane-air}$. Phase injection results in a void at 0.25m that is large enough and has to be scavenged before the configuration can effectively be used. The

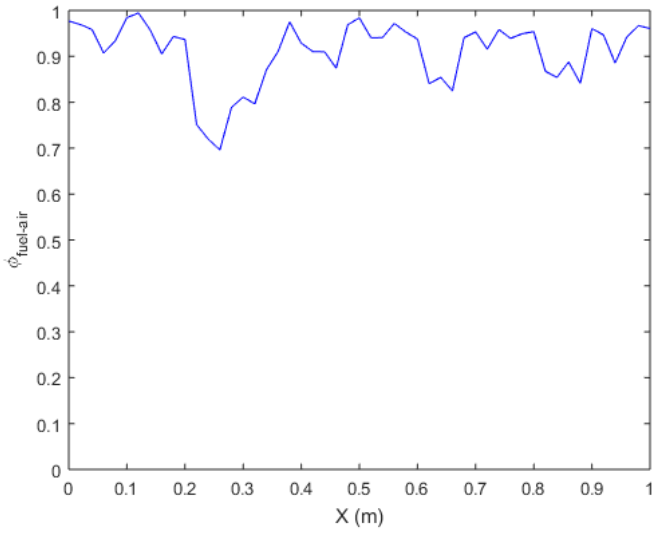

Figure 3.29. $\phi_{biogas-air}$ in streamwise direction of Case 4 with phased injection using volume sweep.

staggered configuration with phased injection does not appear to have improved the fill profile either with time of fill or uniformity.

3.4 Spillage

Non-uniform filling of the detonation tube will inevitably also cause spillage of the reactants. This is a consequence of attempting to fill the tube as much as possible with the reactants. The amount of reactant that is spilled through the open end of the detonation tube if not too large may not significantly affect the performance of a PDE where cycle time and fill uniformity may be more important. Nevertheless, spillage of the combustible mixture can pose an innate safety concern. The volume of spillage can be calculated by taking the difference between the volume of reactants when t_{fill} is reached and the 90 percent volume of the detonation chamber. In order to ease the comparison amongst the various cases, the spillage volume is non-dimensionalized by the volume of chamber. This gives an estimate of the additional volume of reactants

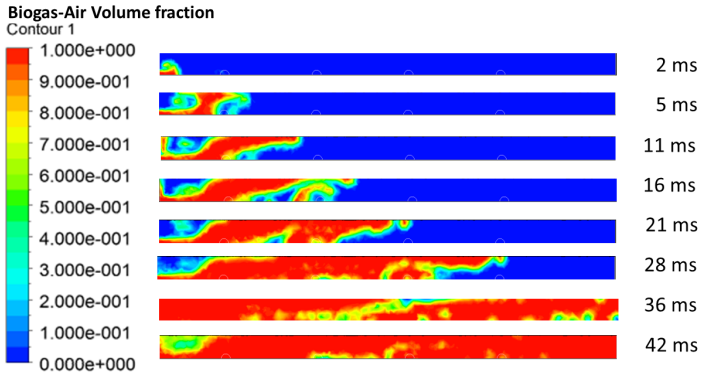

Figure 3.30. Case 4 biogas-air volume fraction at mid-plane with 150 m/s phased injection velocity.

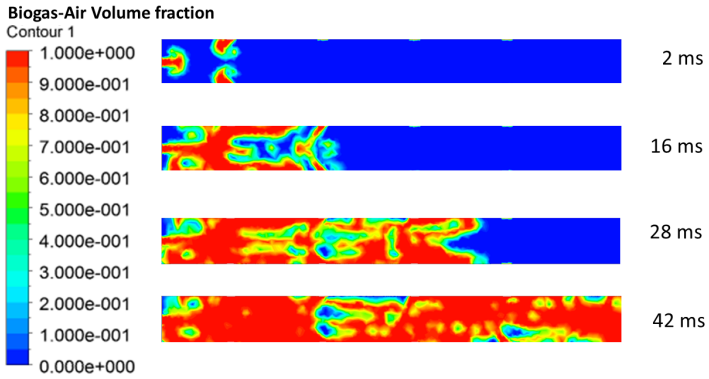

Figure 3.31. Case 4 biogas-air volume fraction at cross section with 150 m/s phased injection velocity.

that has been pumped into the chamber, which is treated the same as the spillage out of engine. Thus, the spillage ratio

$$\varphi = \frac{n d_{inj}^2 V_{inj} t_{fill} - 0.9 d_{ch}^2 L_{ch}}{d_{ch}^2 L_{ch}} = \frac{n d_{inj}^2 V_{inj} t_{fill}}{d_{ch}^2 L_{ch}} - 0.9 \tag{3.2}$$

where n is the number of inlet ports, d_{inj} is the diameter of the injection port,V_{inj} is the velocity of injection, L_{ch} is the length of detonation chamber and d_{ch} is the diameter of detonation chamber. The figure 3.38, shows the spillage ratio for the each of the hydrogen-air mixture.

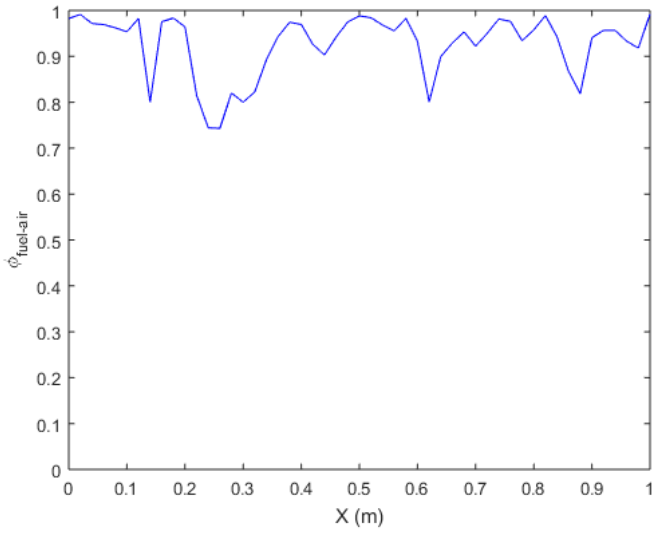

Figure 3.32. $\phi_{octane-air}$ in stream wise direction for Case 5 using volume sweep.

The amount of reactant that is spilled through the open end of the detonation tube is a not a significant factor in PDE applications. PDEs are driven mostly by cycle time and the uniformity of fill. Nevertheless, spillage of combustible mixture can pose an innate safety concern. The spilled combustible mixture may burn uncontrollably. Spillage also represent a waste of reactants. Apart from safety and waste, reducing the spillage will also help in decreasing the fill time as the injected mass of mixture will be filled efficiently.

Unlike the previous section, the discussion here is made between different cases of each fuel–air variation. Figure 3.38 shows that Case 3 has the largest amount of spillage which causes the injected fuel-air mixture to flow through the exit before the overall fill fraction reaches 0.9. Due to the spillage of the mixture, increase in the fill fraction is less than the amount of injected fuel and corresponds to the longest t_{fill}. Figure 3.38 also shows that the end wall configuration has the least spillage. The spillage is around 60 percent of the volume of the chamber. This is followed by Case 2 with nearly 120 percent spillage and Cases 4 and 5 with nearly 150 percent spillage.

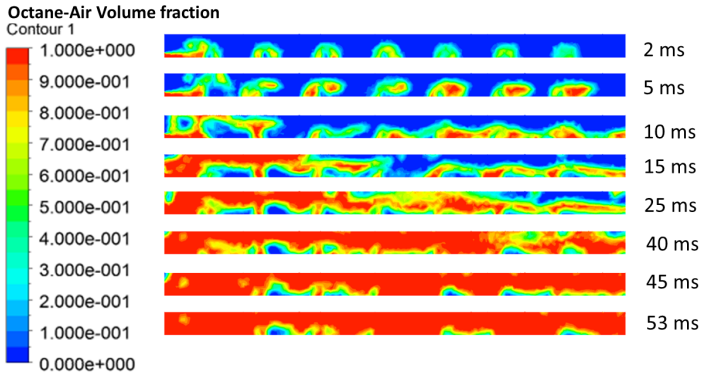

Figure 3.33. Case 5 octane-air volume fraction at mid-plane with 150 m/s injection velocity.

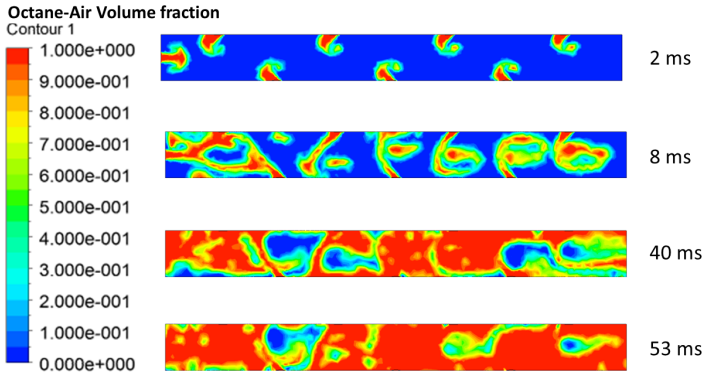

Figure 3.34. Case 5 octane-air volume fraction at cross section with 150 m/s injection velocity.

The spillage for Case 3 shows a large variation from 250–375 percent . This means that a large quantity of reactants is spilled. This could be attributed to injection of mixture inclined towards the downstream direction. This shows that Case 3 is not viable since it has maximum t_{fill} as well as maximum spillage.

To ease further discussion, Case 3 is not considered further. Thus, the plots from Fig. 3.39 through Fig. 3.43 show the spillage for configurations other than Case 3. Figures 3.39–3.43 show spillage for the different injection geometries with each fuel–air mixture configurations. Case 1 has the least spillage but yields the maximum

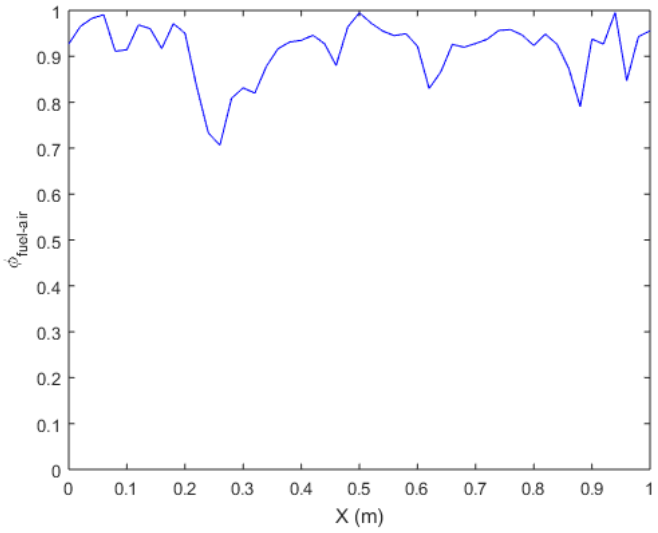

Figure 3.35. $\phi_{octane-air}$ in streamwise direction of Case 5 with phased injection using volume sweep.

t_{fill}. Among these rapid fill configurations, Case 2 has the minimum spillage but which is nearly 140 percent, followed by the Case 4 and Case 5 configurations. The maximum spillage of these configurations were up to 190 percent for propane air mixture. Among the fuels, hydrogen-air mixture has the least spillage for any fill geometry. While the rapid fill geometry of Case 2 has the least spillage, amount spilled is still substantial.

Phased filling of the rapid fill geometries results in significant reduction in the spillage volume as shown in Figs. 3.44–3.47. Except for Case 3, all the other configurations resulted in less than 60 percent of spillage. The least spillage occurs for the Case 2 geometry and is below 20 percent for the hydrogen–air mixture. Thus, in terms of spillage, phased injection improves the filling operation of PDEs.

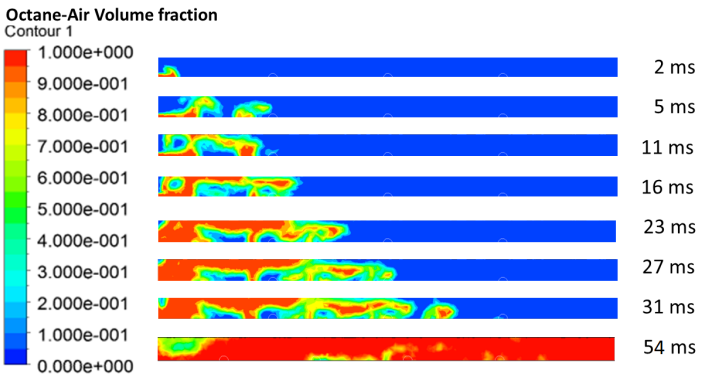

Figure 3.36. Case 5 octane-air volume fraction at mid-plane with 150 m/s phased injection velocity.

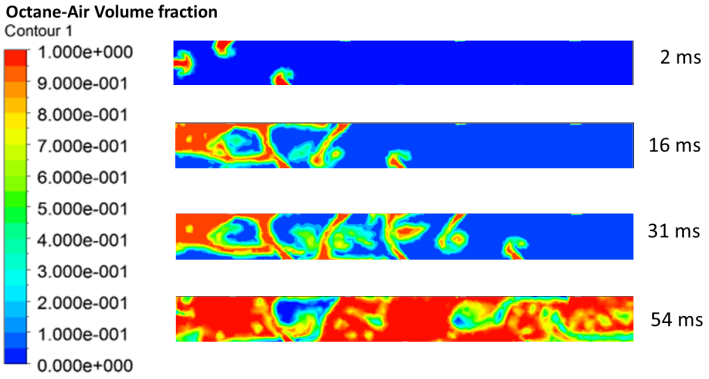

Figure 3.37. Case 5 octane-air volume fraction at cross section with 150 m/s phased injection velocity.

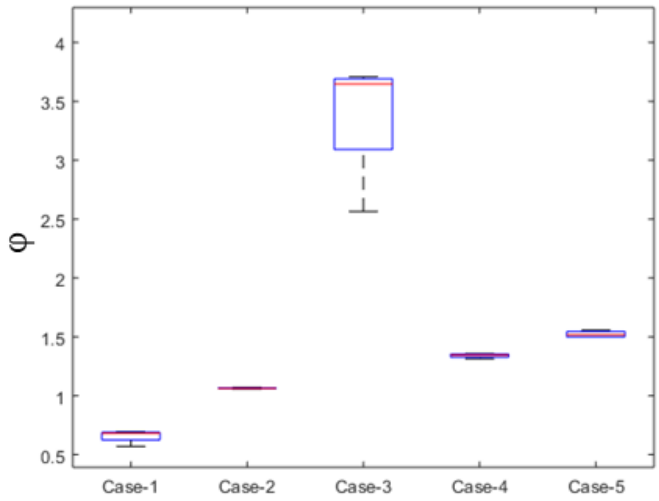

Figure 3.38. Spillage of hydrogen–air for different injection geometries at 50–200 m/s injection velocity.

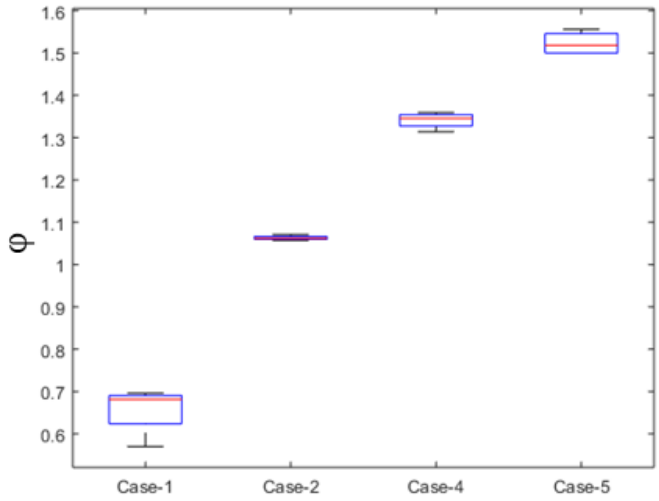

Figure 3.39. Spillage of hydrogen–air for different geometries.

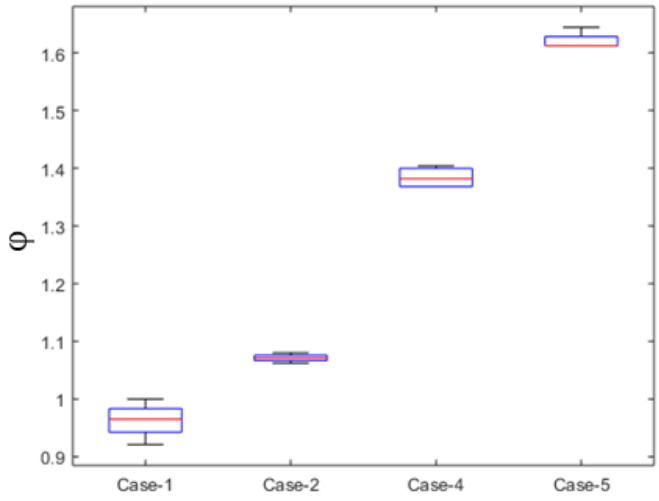

Figure 3.40. Spillage of methane–air for different geometries.

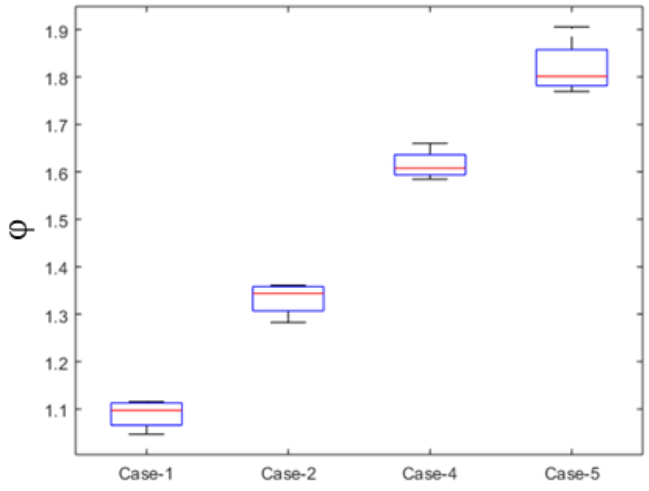

Figure 3.41. Spillage of propane–air for different geometries.

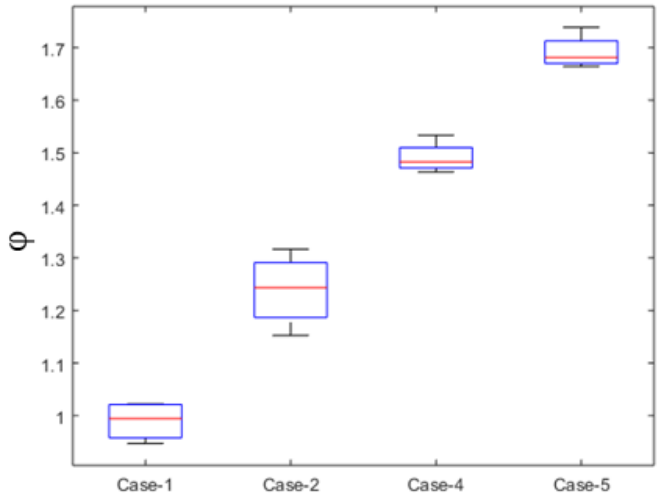

Figure 3.42. Spillage of octane–air for different geometries.

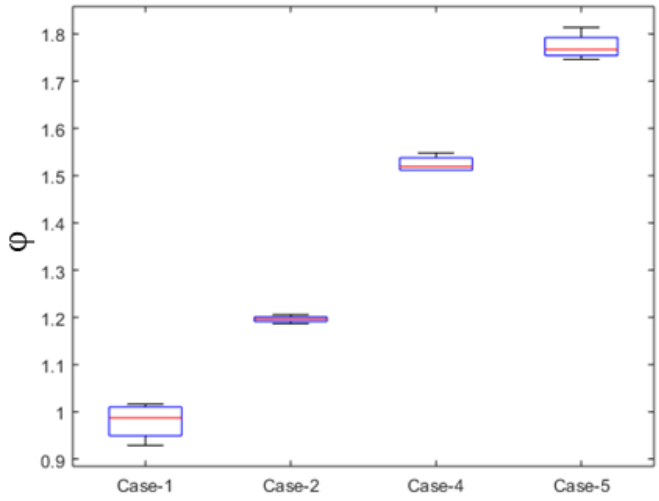

Figure 3.43. Spillage of biogas–air for different geometries.

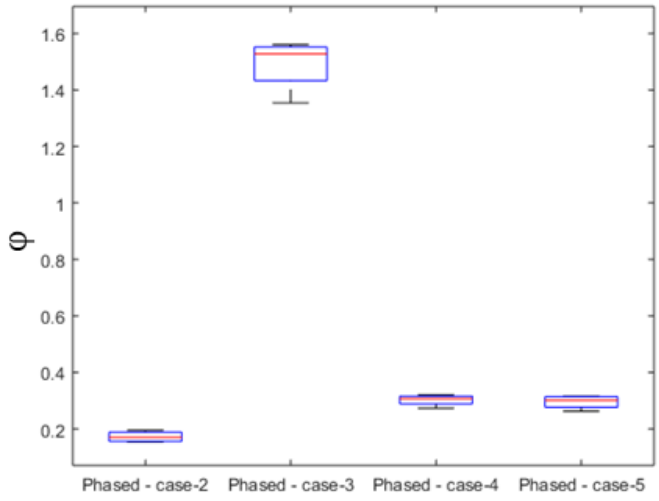

Figure 3.44. Spillage of hydrogen–air for different geometries with phased injection.

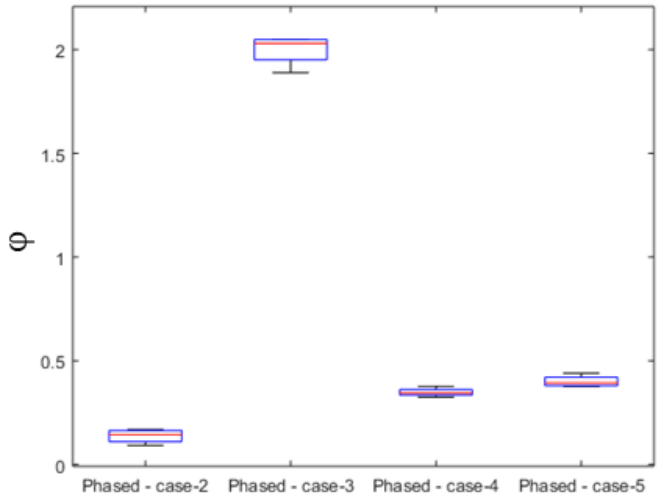

Figure 3.45. Spillage of methane–air for different geometries with phased injection.

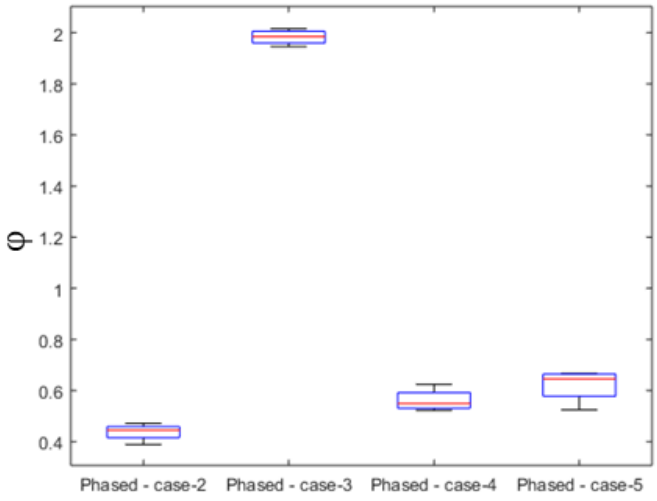

Figure 3.46. Spillage of propane–air for different geometries with phased injection.

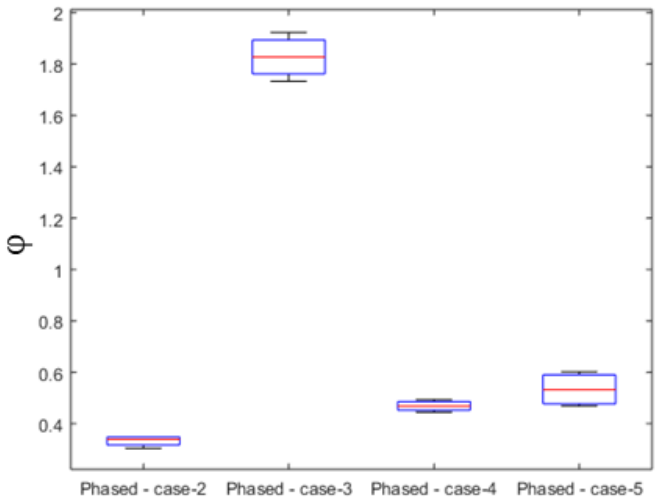

Figure 3.47. Spillage of octane–air for different geometries with phased injection.

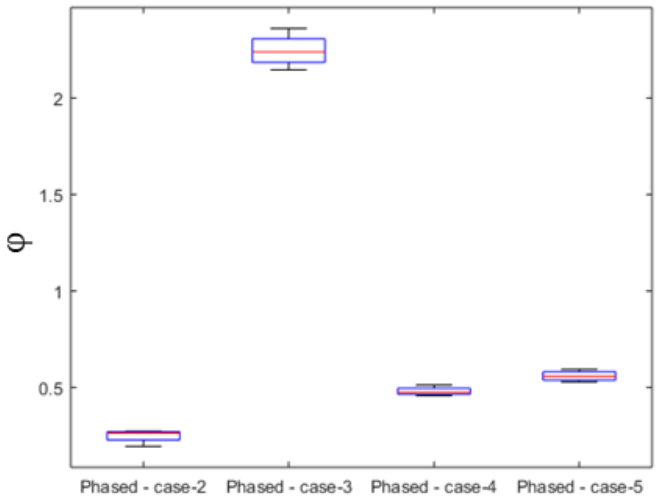

Figure 3.48. Spillage of biogas–air for different geometries with phased injection.

CHAPTER 4

Conclusions

From the current research, it can be concluded that for a specified geometry, phased injection had many advantages as compared to the simultaneous injection. The key parameter that was reduced drastically was the spillage, which would be important in the efficiency and safety of a PDE operation. Also, there was a notable decrease in the time of fill in phased injection regardless of the type of fuel or geometry of injection.

The injection geometry was found to be driven more by the physical aspects of injection such as cross-sectional area, number and location of ports, and velocity and angle of injection. The selection of injection geometry is independent of the fuel–air mixture. Therefore, further studies in filling and purging cycle can be made using a single mixture to optimize the injection configuration. This will help in reducing the computational cost involved in simulating different fuel-air mixtures.

The direction of injection is significant in rapid filling. It was found that injection towards downstream is counter productive. The configurations that has impinging jets result in better filling on the plane of impingement and poor filling in the transverse plane. The staggered configuration has much uniform fill fraction and can be further improved by adding more ports or by changing the placement of injection around the tube.

Among the configurations considered, Case 2 with phased filling provides least fill time and maximum fill efficiency. The next best configuration is Case 4, which has both good fill time and relatively uniform fill fraction across the tube.

Future Scope

As an future attempt, a more generic approach can be made starting with variations in dimensions, then, the location of ports and later the angle of injection. Such a parametric study will help in arriving at an empirical relation for time of fill for any combination of injection geometry. Such a work will be indispensable for designing future PDEs.

Appendix A

Input file for Fluent

```
1  %This journal file imports the case--5 staggered injection ...
       geometry file, sets conditions
2  %that correspond to a 100 m/s flow and runs Implicit solver%
3  %Nirmal Kumar Umapathy%
4
5  file/read-case case5.cas
6  define/boundary-conditions/vi end mixture y y n 100 n 95316 y n 1 ...
       n 0 n 0 y n 1 n 1
7  define/boundary-conditions/vi zone1 mixture y y n 100 n 95316 y n ...
       -0.707 n -0.707 n 0 y n 1 n 1
8  define/boundary-conditions/vi zone2 mixture y y n 100 n 95316 y n ...
       -0.707 n 0.707 n 0 y n 1 n 1
9  define/boundary-conditions/vi zone3 mixture y y n 0 n 101325 y n ...
       -0.707 n -0.707 n 0 y n 1 n 1
10 define/boundary-conditions/vi zone4 mixture y y n 0 n 101325 y n ...
       -0.707 n 0.707 n 0 y n 1 n 1
11 define/boundary-conditions/vi zone5 mixture y y n 0 n 101325 y n ...
       -0.707 n -0.707 n 0 y n 1 n 1
12 define/boundary-conditions/vi zone6 mixture y y n 0 n 101325 y n ...
       -0.707 n 0.707 n 0 y n 1 n 1
13 define/boundary-conditions/vi zone7 mixture y y n 0 n 101325 y n ...
       -0.707 n -0.707 n 0 y n 1 n 1
14 solve/initialize/h
15 solve/patch h fluid () mp 0
```

```
16 solve/m/v/s/hydrogen-case5 Volume-Average h vof fluid () n n y ...
       hydrogen-timed-case5-2 1 y f
17 file/write-case case5phased-1.cas
18 file/write-data case5phased-1.dat
19 file/auto-save/data-frequency 5
20 file/auto-save/case-frequency/if-case-is-modified
21 file/auto-save/retain-most-recent
22 file/auto-save/append-file-name-with/time-step 5
23 solve/set/time-step 0.00025
24 solve/dual-time-iterate 70 300
25 define/boundary-conditions/vi zone3 mixture y y n 100 n 95316 y n ...
       -0.707 n -0.707 n 0 y n 1 n 1
26 solve/dual-time-iterate 18 300
27 define/boundary-conditions/vi zone4 mixture y y n 100 n 95316 y n ...
       -0.707 n 0.707 n 0 y n 1 n 1
28 solve/dual-time-iterate 15 300
29 define/boundary-conditions/vi zone5 mixture y y n 100 n 95316 y n ...
       -0.707 n -0.707 n 0 y n 1 n 1
30 solve/dual-time-iterate 13 300
31 define/boundary-conditions/vi zone6 mixture y y n 100 n 95316 y n ...
       -0.707 n 0.707 n 0 y n 1 n 1
32 solve/dual-time-iterate 12 300
33 define/boundary-conditions/vi zone7 mixture y y n 100 n 95316 y n ...
       -0.707 n -0.707 n 0 y n 1 n 1
34 solve/dual-time-iterate 100 300
35 file/case-data case5phased-2f.cas
36 file/write-data case5phased-2f.dat
```

Appendix B

Matlab script for fill time plot

```
clc;
clear;
M=dlmread('hydrogen_timed_case5_3',' ',2,0);
V=((0.01^2)*100*M(:,1))*3/0.05^2; % ideal Volume
[m,n]=find(M(:,2)>0.895,1,'first');
ti9=M(m,1);
sev=([ti9,ti9,0]);
sevy=([0,0.9,0.9]);
[m8,n8]=find(M(:,2)>0.8,1,'first');
ti8=M(m8,1);
sev8=([ti8,ti8,0]);
sevy8=([0,0.8,0.8]);
[m7,n7]=find(M(:,2)>0.7,1,'first');
ti7=M(m7,1);
sev7=([ti7,ti7,0]);
sevy7=([0,0.7,0.7]);
plot(M(:,1),M(:,2),'-',sev,sevy,'--',sev8,sevy8,'--',sev7,sevy7....
    .....,'--',M(:,1),V,'--','marker','none');
%plot(M(1:600,1),M(1:600,2),sev,sevy,M(:,1),V,'--','marker','none');
%plot(M(1:600,1),M(1:600,2),sev,sevy,'--','marker','none');
axis([0 (ti9+(0.5*ti9)) 0 1.1]);
xlabel('Time (sec)');
ylabel('\phi_{fuel-air}');
%title('Volume of fill vs Time');
```

```
legend('\phi_{Propane--air}','\phi = 0.9','\phi = 0.8','\phi = ...
    0.7',...
     ....'location','southeast');
%legend('\phi_{hyd--air}','\phi = 0.9','location','southeast');
```

Matlab script for volume sweep

```
%post processing for quality
clear;
clc;
file='case4.csv';
M=dlmread(file,' ',7,0);
Node(:,1)=M(:,1);
co(:,1:3)=M(:,2:4);
vf(:,1)=M(:,5);
Tr=delaunayTriangulation(co(:,1),co(:,2),co(:,3));
[m,n]=size(co);
for i=1:m;
    X(i,1)=round(co(i,1),2);
   end
for i=1:51;%extracting data
    coun=0;
    var=0;
    for j=1:m;
    if X(j,1)==round((i-1)*0.02,2);
        coun=coun+1;
        var=var+vf(j);
    else
        var=var;
```

```
23      end
24      end
25      Volfrac(i)=var/(coun);
26  end
27  VF=sum(Volfrac)/51;%cross check
28  plot(0:0.02:1,Volfrac,'b');
29  % f=fit([0:0.02:1]',Volfrac','smoothingspline');
30  % plot(f,0:0.02:1,Volfrac);
31  axis([0 1 0 1]);
32  ylabel('\phi_{fuel-air}');
33  xlabel('X (m)');
34  legend off;
```

REFERENCES

[1] Lee, J. H. S., 2008. *The Detonation Phenomenon.* Cambridge, New York.

[2] Lu, F. K., 2010. "Prospects for detonation propulsion". In invited lecture, 9th International Symposium on Experimental and Computational Aerothermodynamics of Internal Flows, September 8–11, 2009, GyeongJu, Korea.

[3] Kailasanath, K., 1999. "A review of research on pulse detonation engines". In Proceedings of the 17th International Colloquium on the Dynamics of Explosion and Reactive Systems.

[4] Fan, H. Y., and Lu, F. K., 2008. "Numerical modelling of oblique shock and detonation waves induced in a wedged channel". *Journal of Aerospace Engineering,* **222**(5), pp. 687–703.

[5] Nicholls, J. A., Wilkinson, H. R., and Morrison, R. B., 1957. "Intermittent detonation as a thrust-producing mechanism". *Jet Propulsion,* **27**(5), pp. 534–541.

[6] Cambier, J.-L., Adelman, H., and Menees, G. P., 1990. "Numerical simulations of an oblique detonation wave engine". *Journal of Propulsion and Power,* **6**(3), pp. 315–323.

[7] Bussing, T. R. A., and Pappas, G., 1996. *Pulse Detonation Engine Theory and Concepts*, Vol. 165 of *Progress in Aeronautics and Astronautics.* AIAA, Reston, Virginia, pp. 421–472.

[8] Lu, F. K., and Braun, E. M., 2014. "Rotating detonation wave propulsion: experimental challenges, modeling, and engine concepts". *Journal of Propulsion and Power,* **30**, pp. 1125–1142.

[9] Bussing, T., and Pappas, G., 1994. "An introduction to pulse detonation engines". Aerospace Sciences Meetings. American Institute of Aeronautics and Astronautics, Jan.

[10] Fickett, W., and Davis, W. C., 2001. *Detonation Theory and Experiment.* Dover, Mineola, New York.

[11] Wu, Y., Ma, F., and Yang, V., 2003. "System performance and thermodynamic cycle analysis of airbreathing pulse-detonation engines". *Journal of Propulsion and Power,* **19**(4), pp. 556–567.

[12] Snyder, C. A., 2016. Chemical equilibrium with applications, Feb. [Accessed 15 August 2016].

[13] Coleman, M., 2010. Overview of pulse detonation propulsion technology. Tech. rep., Chemical Propulsion Information Agency, Columbia, Maryland.

[14] Lu, F. K., Carter, J. D., and Wilson, D. R., 2011. Development of a large pulse detonation engine demonstrator. AIAA Paper 2011–5544. 47th AIAA/ASME/SAE/ASEE Joint Propulsion Conference and Exhibit, San Diego, California, July 31-August 3, 2011.

[15] Chandran, S., 2015. "Multiphase flow modeling and analysis of filling process for pulsed detonation engines". Master's thesis, University of Texas at Arlington.

[16] Tabor, G., 2010. "Computational fluid dynamics, multiphase flow modelling".

[17] "ohne, T. H., 2010. CFD simulations for single and multi-phase flows. Institute of Safety Research, Dresden-Rossendorf, Germany, March. Lecture notes, FZD Theory Seminar Series.

[18] Rudman, M., 1997. "Volume-tracking volume for interfacial flow calculations". *International Journal for Numerical Methods in Fluids,* **24**, Apr, p. 671.

[19] Denner, F., 2014. "Compressive vof method with skewness correction to capture sharp interfaces on arbitrary meshes". *Journal of computational physics,* **279**, dec, p. 127.

[20] Anon., 2013. Ansys fluent user's guide, release 15.0. Tech. rep., ANSYS, Inc.

[21] Ubbink, O., and Issa, R. I., 1999. "A Method for Capturing Sharp Fluid Interfaces on Arbitrary Meshes". *Journal of Computational Physics,* **153**, July, pp. 26–50.

[22] Andersson, B., Andersson, R., Hkansson, L., Mortensen, M., Sudiyo, R., and van Wachem, B., 2012. *Computational Fluid Dynamics for Engineers*. CAMBRIDGE UNIVERSITY PRESS.

[23] Versteeg, H. K., and Malalasekera, W., 2007. *An Introduction to Computational Fluid Dynamics: The Finite Volume Method*. Pearson Education Limited.

[24] Bradshaw, P., 1987. "Turbulent secondary flows". *Annu. Rev. Fluid Mech.,* **19**(1), Jan., pp. 53–74.

[25] Lu, F. K., Umapathy, N. K., and Thirumangalath, S. C., 2017. "Multi-port filling of pulsed detonation engines". International Space Planes and Hypersonic Systems and Technologies Conferences. American Institute of Aeronautics and Astronautics, Mar.

[26] Hunter, L. G., and Winfree, D. D., 1996. Pulse detonation apparatus with spherical seals. U.S. Patent No. 5,546,744.

[27] Castillo, J. E., 1991. Mathematical aspects of numerical grid generation, Jan.

[28] Sack, J. R., and Urrutia, J., 1999. *Handbook of Computational Geometry*. Elsevier Science.

[29] Young, D. M., 1971. *Iterative solution of large linear systems*. Computer science and applied mathematics. Academic Press.

[30] Butcher, J. C., 1987. *The numerical analysis of ordinary differential equations: Runge-Kutta and general linear methods*. Wiley-Interscience publication. J. Wiley.

[31] Patankar, S., 1980. Numerical heat transfer and fluid flow.

[32] Office of Information Technology, The University of Texas at Arlington, 2017. *HPC Users Guide*, Jan.

[33] Texas Advanced Computing Center, The University of Texas at Austin, 2017. *Stampede User Guide*, Apr.

[34] , 2013. Ansys fluent text command list. Online, Nov.

[35] Anon., 2006. Fluent 6.3 tutorial guide. Tech. rep., Fluent Inc.